JBC ARTICLE

Structural control of caspase-generated glutamyl-tRNA synthetase by appended noncatalytic WHEP domains

Received for publication, July 19, 2017, and in revised form, March 26, 2018 Published, Papers in Press, April 11, 2018, DOI 10.1074/jbc.M117.807503

Dalia Halawani[‡], Valentin Gogonea[‡§1], Joseph A. DiDonato[‡], Vitaliy Pipich[¶], Peng Yao[‖], Arnab China[‡], Celalettin Topbas[‡§], Kommireddy Vasu[‡], Abul Arif[‡], Stanley L. Hazen[‡**], and Paul L. Fox[‡2]

*From the [‡]Department of Cellular and Molecular Medicine, Lerner Research Institute and **Center for Cardiovascular Diagnostics and Prevention, and Department of Cardiovascular Medicine, Cleveland Clinic Foundation, Cleveland, Ohio 44195, the [§]Department of Chemistry, Cleveland State University, Cleveland, Ohio 44115, the [¶]Jülich Center for Neutron Science, Outstation at Maier-Leibnitz Zentrum, Forschungszentrum Jülich, GmbH, Lichtenbergstrasse 1, 85747 Garching, Germany, and the [‖]Department of Medicine, Aab Cardiovascular Research Institute, University of Rochester, Rochester, New York 14642*

Edited by Norma M. Allewell

Aminoacyl-tRNA synthetases are ubiquitous, evolutionarily conserved enzymes catalyzing the conjugation of amino acids onto cognate tRNAs. During eukaryotic evolution, tRNA synthetases have been the targets of persistent structural modifications. These modifications can be additive, as in the evolutionary acquisition of noncatalytic domains, or subtractive, as in the generation of truncated variants through regulated mechanisms such as proteolytic processing, alternative splicing, or coding region polyadenylation. A unique variant is the human glutamyl-prolyl-tRNA synthetase (EPRS) consisting of two fused synthetases joined by a linker containing three copies of the WHEP domain (termed by its presence in tryptophanyl-, histidyl-, and glutamyl-prolyl-tRNA synthetases). Here, we identify site-selective proteolysis as a mechanism that severs the linkage between the EPRS synthetases *in vitro* and *in vivo*. Caspase action targeted Asp-929 in the third WHEP domain, thereby separating the two synthetases. Using a neoepitope antibody directed against the newly exposed C terminus, we demonstrate EPRS cleavage at Asp-929 *in vitro* and *in vivo*. Biochemical and biophysical characterizations of the N-terminally generated EPRS proteoform containing the glutamyl-tRNA synthetase and most of the linker, including two WHEP domains, combined with structural analysis by small-angle neutron scattering, revealed a role for the WHEP domains in modulating conformations of the catalytic core and GSH–*S*-transferase–C-terminal-like (GST-C) domain. WHEP-driven conformational rearrangement altered GST–C domain interactions and conferred distinct oligomeric states in solution. Collectively, our results reveal long-range conformational changes imposed by the WHEP domains and illustrate how noncatalytic domains can modulate the global structure of tRNA synthetases in complex eukaryotic systems.

In all three kingdoms of life, the initial step of protein synthesis, *i.e.* tRNA aminoacylation, relies on the catalytic activity and accuracy of aminoacyl-tRNA synthetases (AARSs).[3] These ancient enzymes comprise a catalytic core and catalyze the conjugation of amino acids onto the 3′ end of cognate tRNAs, thereby generating the cellular repertoire of charged aminoacyl-tRNAs used by translating ribosomes (1, 2). In higher eukaryotes, many synthetases have acquired a spectrum of orthogonal functions critical for cell survival and homeostasis, which include regulation of apoptosis (3, 4), gene transcription (5), mRNA translation (6, 7), RNA splicing (8), and amino acid-sensing (9, 10). These diverse biological activities are enabled by distinct structural adaptations, which facilitate the repurposing of tRNA synthetases in alternative pathways. Whereas some noncanonical functions are mediated by full-length synthetases, in other cases truncated protein variants generated by regulated mechanisms such as proteolytic processing (11), alternative-splicing (12, 13), or coding-region polyadenylation (14), mediate noncanonical activities. In addition, structural adaptations of tRNA synthetases can be conferred by evolutionary acquisition of eukaryote-specific, noncatalytic domains, of which 13 have been described, including the WHEP, GSH–*S*-transferase–C-terminal–like (GST-C), UNE-S

This work was supported by National Institutes of Health Grants P01 HL029582, P01 HL076491, R01 GM086430, and R01 GM115476 (to P. L. F.) Grant R01 HL128300 (to S. L. H.), and Grant R01 HL128268, by American Heart Association National Center Scientist Development Grant 10SDG3930003 (to A. A.), by a Canadian Institute of Health Research Fellowship (to D. H.), and by an American Heart Association Fellowship Award 15POST22450016 (to K. V.). The authors declare that they have no conflicts of interest with the contents of this article. The content is solely the responsibility of the authors and does not necessarily represent the official views of the National Institutes of Health.

This article contains Figs. S1–S3 and Tables S1 and S2.

[1] Supported by Cleveland State University through the Faculty Scholarship Initiative and Faculty Research Development Awards. To whom correspondence may be addressed: Dept. of Chemistry, Cleveland State University, Cleveland, OH 44115. Tel.: 216-87-9717; Fax: 216-687-9298; E-mail: v.gogonea@csuohio.edu.

[2] To whom correspondence may be addressed: Dept. of Cellular and Molecular Medicine, Lerner Research Institute, Cleveland Clinic, 9500 Euclid Ave., Cleveland, OH 44195. Tel.: 216-444-8053; Fax: 216-444-9404; E-mail: foxp@ccf.org.

[3] The abbreviations used are: AARS, aminoacyl-tRNA synthetase; EPRS, glutamyl-prolyl-tRNA synthetase; GST-C, GSH–*S*-transferase-C-terminal-like; MST, microscale thermophoresis; DAPI, 4′,6-diamidino-2-phenylindole; Z-VAD-FMK, benzyloxycarbonyl; FMK, fluoromethyl ketone; CHX, cycloheximide; MRS, methionyl-tRNA synthetase; WRS, tryptophanyl-tRNA synthetase; HRS, histidyl-tRNA synthetase; GRS, glycyl-tRNA synthetase; PRS, prolyl-tRNA synthetase; IRS, isoleucyl-tRNA synthetase; KRS, lysyl–tRNA synthetase; SANS, small-angle neutron scattering; SEC, size-exclusion chromatography; FBS, fetal bovine serum; TNFα, tumor necrosis factor α; PARP, poly(ADP-ribose) polymerase; EC, exchange chromatography; GAIT, γ-interferon–activated inhibitor of translation.

Downloaded from http://www.jbc.org/ at Rsch Cntr Julich Res library on November 22, 2018

© 2018 by The American Society for Biochemistry and Molecular Biology, Inc. Published in the U.S.A.

domains, and others (15). Whether subtractive or additive, structural modifications of tRNA synthetases represent a crucial feature of their evolution and function in eukaryotes.

The WHEP domain is a 46-amino acid helix-turn-helix found only in eukaryotic AARSs. A single copy is appended to the N terminus of tryptophanyl- (WRS), histidyl- (HRS), and glycyl (GRS)-tRNA synthetases and to the C terminus of methionyl (MRS)-tRNA synthetase, but it is expanded to three copies in the central region of the glutamyl-prolyl (EPRS)-tRNA synthetase. WHEP domains have been implicated in the regulation of multiple physiological and pathophysiological activities. For example, deletion of the WRS WHEP domain results in a conformational rearrangement allowing the tryptophan-binding pocket to engage tryptophan residues on vascular endothelial-cadherins to inhibit endothelial cell migration (16). The HRS WHEP domain exhibits immunogenic epitopes for production of autoimmune antibodies implicated in the pathogenesis of polymyositis, dermatomyositis, and interstitial lung disease and induces lymphocyte migration and macrophage activation (17, 18). Recently, the HRS WHEP domain was implicated in conformational rearrangement of the anticodon–binding domain of a novel, and potentially pathogenic, splice variant lacking the catalytic core (19). The GRS WHEP domain contributes to pathogenicity of mutants associated with neurodegeneration, although the domain itself is devoid of disease-associated mutations (20). Phosphorylation of the MRS WHEP domain during oxidative stress increases its promiscuity for noncognate tRNA, thereby altering global translational fidelity (21). Common to all of these examples is the observation that the physiological and deleterious effects of the WHEP domain are mediated by structural mechanisms influencing the catalytic core or tRNA-binding domain of its associated synthetase.

The glutamyl-tRNA synthetase (ERS) exists in various forms that increase in structural complexity ascending the evolutionary tree. The prototypical prokaryotic ERS is a monomer belonging to the class I family of AARSs, consisting of a catalytic core and tRNA-binding domain (22). In eukaryotes, ERS progressively acquired appended noncatalytic domains, including the GST–C domain in yeast and a C-terminal WHEP domain in *Sphaeroforma arctica*, a unicellular icthyosporean animal (23). The earliest known organism in which ERS is fused to prolyl-tRNA synthetase (PRS) is *Capsaspora owczarzaki*, a unicellular filasterean animal (23). In *Capsaspora*, ERS is joined to PRS by a linker containing two WHEP domains (23) to form EPRS, the only known bifunctional tRNA synthetase (24). The two synthetases have remained fused in vertebrates and invertebrates, with the exception of *Caenorhabditis elegans* in which a fission event restored the individual synthetases, both bearing WHEP domains (23). Currently, little is known about the regulation of EPRS canonical activity and whether the activities of the synthetases are functionally linked. In addition to its dual canonical activities, EPRS mediates several noncanonical functions in higher eukaryotes through its appended noncatalytic domains (6, 7, 25–27). For example, the GST–C domain mediates an anti-viral activity of EPRS by regulating its interaction with poly(rC)-binding protein 2 (PCBP2), a negative regulator of the mitochondrial antiviral signaling pathway (26). In contrast, the WHEP-containing linker promotes transcript-selective translational control of gene expression in interferon-γ–activated myeloid cells by binding inflammation-related target mRNAs and by serving as a scaffold for other protein constituents of the heterotetrameric γ-interferon–activated inhibitor of translation (GAIT) system (28). More recently, the EPRS linker was shown to bind fatty acid transport protein 1 (FATP1) and transport it to plasma membranes to facilitate fatty acid uptake in insulin-treated adipocytes (27). Common to all of these noncanonical functions is the stimulus-dependent release of EPRS from the tRNA multisynthetase complex (MSC) via linker phosphorylation (26, 29). In contrast to other WHEP domain-bearing synthetases, little is known about the structural influence of these domains on the conformation of its associated glutamyl- or prolyl-tRNA synthetases.

Proteolytic cleavage of MSC components has been previously demonstrated and proposed to regulate the canonical and noncanonical functions of MSC synthetases and scaffolding proteins (30, 31). EPRS has been shown to be a proteolytic target of caspase and calpain activity *in vitro*; however, neither the cleavage event nor the resulting structural alteration has been characterized (30–33). Caspases are cysteine-dependent aspartic acid proteases that cleave after aspartate (or rarely glutamate) residues and are crucial for regulation of cell death and differentiation, as well as inflammation (34). Here, we characterize EPRS cleavage by caspases and identify ^{926}DQVD^{929} as the preferential caspase cleavage site. EPRS cleavage bisects the protein into its two constituent synthetase fragments. Using small-angle neutron scattering, we resolve the solution structure of the N-terminal fragment containing the glutamyl-tRNA synthetase and two complete and one partial WHEP domain. Overall, our results provide insights into the functional complexity of the WHEP domain and highlight its contribution as a regulator of the global conformational state of its parental synthetase.

Results

Site-selective cleavage of EPRS uncouples the glutamyl- and prolyl-tRNA synthetases

EPRS is the largest human tRNA synthetase, containing an N-terminal ERS domain joined to a C-terminal PRS domain by an internal linker containing a triple repeat of noncatalytic WHEP domains (Fig. 1*A*). In addition, a GST–C domain is appended to the N terminus of ERS. Computational analysis of the human EPRS sequence (NP_004437.2) revealed five putative caspase cleavage sites: ^{448}GWDD^{451}, ^{770}EDVD^{773}, ^{926}DQVD^{929}, ^{1062}DFFD^{1065}, and ^{1344}DLRD^{1347}, each with a cleavage score exceeding 0.9 (Fig. 1*A*, *arrows*). To experimentally determine cleavage sites, cytoplasmic extracts of HEK293F cells overexpressing N-terminally FLAG-tagged EPRS were treated with active recombinant caspase-3 *in vitro*. Caspase-3–mediated cleavage of FLAG-tagged EPRS was detected with antibodies recognizing epitopes within the FLAG peptide, linker sequence, or PRS domain. Caspase-3 generated a ~100-kDa fragment detected by anti-FLAG–tag antibody (Fig. 1*B*, *left panel*). The fragment size is consistent with the entire ERS domain and part of the linker. Probing with the linker antibody

Downloaded from http://www.jbc.org/ at Rsch Cntr Julich Res library on November 22, 2018

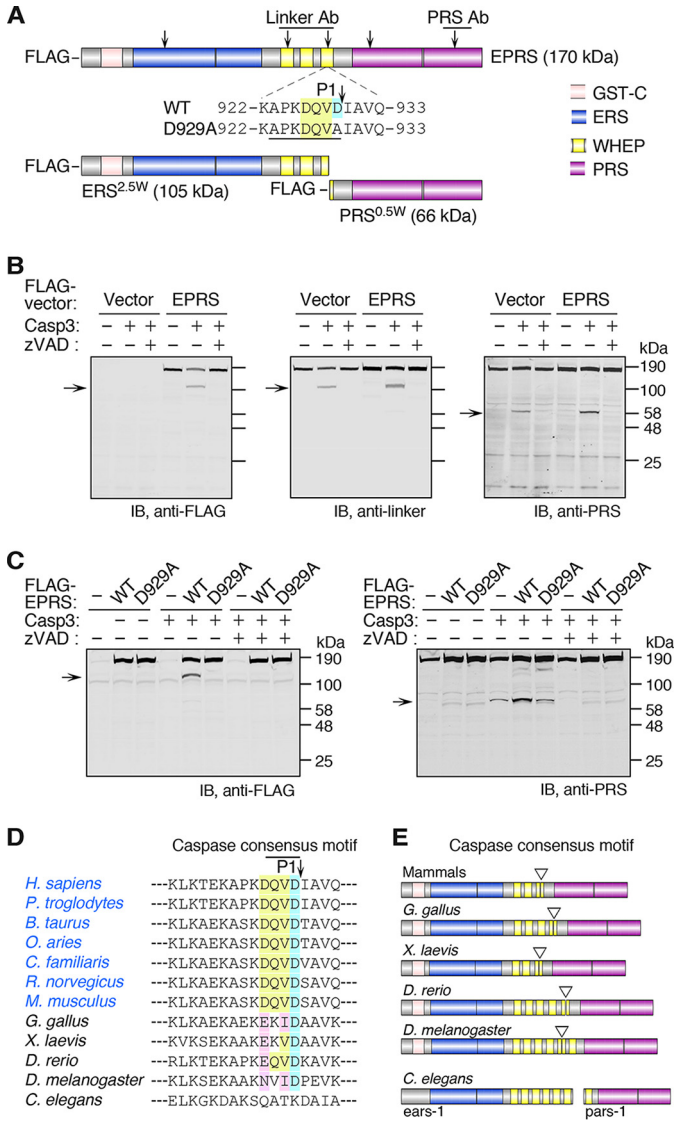

Figure 1. ^{926}DQVD^{929} is a functional and evolutionarily conserved caspase-cleavage site in EPRS. *A,* domain organization of human EPRS and two caspase-generated fragments, ERS$^{2.5W}$ and PRS$^{0.5W}$. *Arrows* indicate predicted caspase cleavage sites. Epitopes for domain- or tag-specific antibodies are indicated. Sequence and localization of the caspase cleavage site, DQVD^{929}, are shown. Peptide used for neoepitope antibody generation is *underlined*. *B,* quantitative Western blot analysis of transfected HEK293F lysates treated with recombinant caspase-3 (*Casp3*) in the presence or absence of Z-VAD (20 μM) and probed with domain- or tag-specific EPRS antibodies. *C,* quantitative Western blot analysis of EPRS^{WT}- or EPRS^{D929A}-transfected HEK293F lysates treated with recombinant caspase-3 in the presence or absence of Z-VAD (20 μM). *D,* multiple sequence alignment of the region containing the caspase-cleavage site in EPRS. *Blue, yellow,* and *magenta* denote the P1 aspartic acid and conserved and similar amino acid substitutions, respectively. Mammalian species are indicated in *blue*. *E,* domain organization of EPRS in multiple species and of ears-1 and pars-1 in *C. elegans*. *Open arrowheads* indicate the conserved caspase-cleavage site.

confirmed the 100-kDa fragment and also showed cleavage of endogenous, as well as overexpressed, EPRS (Fig. 1*B*, *middle panel*). An antibody targeting PRS (Fig. 1*A*) revealed a 60–65-kDa C-terminal fragment likely to include the entire 58-kDa PRS (Fig. 1*B*, *right panel*). Thus, caspase-3 appears to cleave at a single site in the EPRS linker that yields segments containing both intact synthetases. Generation of both fragments was abolished by treatment with the pan-caspase inhibitor, Z-VAD-FMK (Z-VAD), confirming cleavage dependence on caspase activity (Fig. 1*B*).

The size of the fragments generated by caspase-3 is consistent with ^{926}DQVD^{929} within the linker as a candidate cleavage site, which would generate 105- and 66-kDa fragments (Fig. 1*A*). The 105-kDa N-terminal fragment contains the glutamyl-tRNA synthetase and the first two WHEP domains and about half of the third (termed ERS$^{2.5W}$), and the 66-kDa C-terminal fragment contains the remaining half-WHEP domain appended upstream of the PRS (termed PRS$^{0.5W}$). To confirm this site, we mutated the critical P1 position residue, Asp-929, to alanine (D929A) and assessed susceptibility to caspase cleavage. Generation of the 105-kDa N-terminal (Fig. 1*C*, *left panel*) and 66-kDa C-terminal (Fig. 1*C*, *right panel*) fragments was abolished in the mutant, identifying ^{926}DQVD^{929} as a caspase cleavage site that severs the linkage between ERS and PRS.

The ^{926}DQVD^{929} sequence is conserved in all mammalian species examined, from mouse to human, and is potentially indicative of a functional significance (Fig. 1*D*). ^{926}DQVD^{929} is localized within the third WHEP domain of humans and other mammals (Fig. 1*E*). Although not identical, *Drosophila*, zebrafish, *Xenopus*, and chicken contain potential caspase cleavage sites, with conservation of the critical P1 aspartate. Interestingly, the caspase cleavage site was lost in *C. elegans*, an organism in which the separate ERS and PRS proteins are encoded by two distinct genes, *ears-1* and *pars-1* (Fig. 1*D*). In all species examined, the caspase cleavage site was present in the C-terminal WHEP repeat, with the exception of *Drosophila*, where it localized to the penultimate WHEP domain (Fig. 1*E*). In *C. elegans*, six WHEP repeats are also fused to the C terminus of ERS. These results suggest that caspase activity may represent an evolutionarily conserved mechanism for inducible separation of ERS and PRS and the generation of novel WHEP domain-containing EPRS proteoforms in mammalian cells.

Catalytic activity of ERS$^{2.5W}$ and PRS$^{0.5W}$ and their association with the MSC

AARSs catalyze the conjugation of amino acids onto the 3′ end of tRNAs by a reversible two-step reaction. The amino acid is first condensed with ATP to yield an aminoacyl-adenylate intermediate accompanied by release of pyrophosphate. In the second step, the aminoacyl-adenylate is transferred onto the tRNA to form a charged aminoacyl-tRNA. To determine whether the cleavage products retained limited catalytic activities, we purified recombinant His-tagged ERS$^{2.5W}$ and PRS$^{0.5W}$ and measured the terminal step of their aminoacylation activities *in vitro* (Fig. 2, *A* and *B*). ERS$^{2.5W}$ purified primarily as a single band with only minor contaminants, and under the conditions used (1 μM of purified enzyme), displayed very weak catalytic activity (Fig. 2*A*). In contrast, PRS$^{0.5W}$ catalyzed time-dependent conjugation of L-[^{14}C]proline on yeast tRNA using 50 nM purified enzyme (Fig. 2*B*). Comparison with full-length EPRS activity was not possible because efforts to purify full-length protein from bacterial expression systems were not successful.

We next tested the ability of the EPRS fragments (Fig. 3*A*) to interact with EPRS or MSC components by co-immunoprecipitation (Fig. 3*B*). As expected, FLAG-tagged EPRS pulled down

Downloaded from http://www.jbc.org/ at Rsch Cntr Julich Res library on November 22, 2018

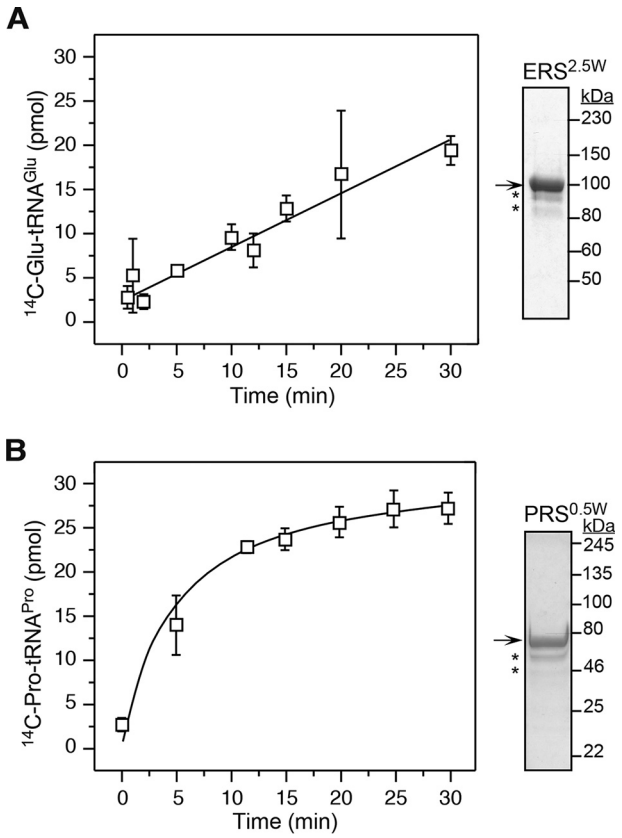

Figure 2. Catalytic activity of ERS$^{2.5W}$ and PRS$^{0.5W}$. *A* and *B*, aminoacylation activity of purified recombinant ERS$^{2.5W}$ (*A*) and PRS$^{0.5W}$ (*B*). Purified ERS$^{2.5W}$ and PRS$^{0.5W}$ on Coomassie-stained SDS-polyacrylamide gel are shown at the *right panel*.

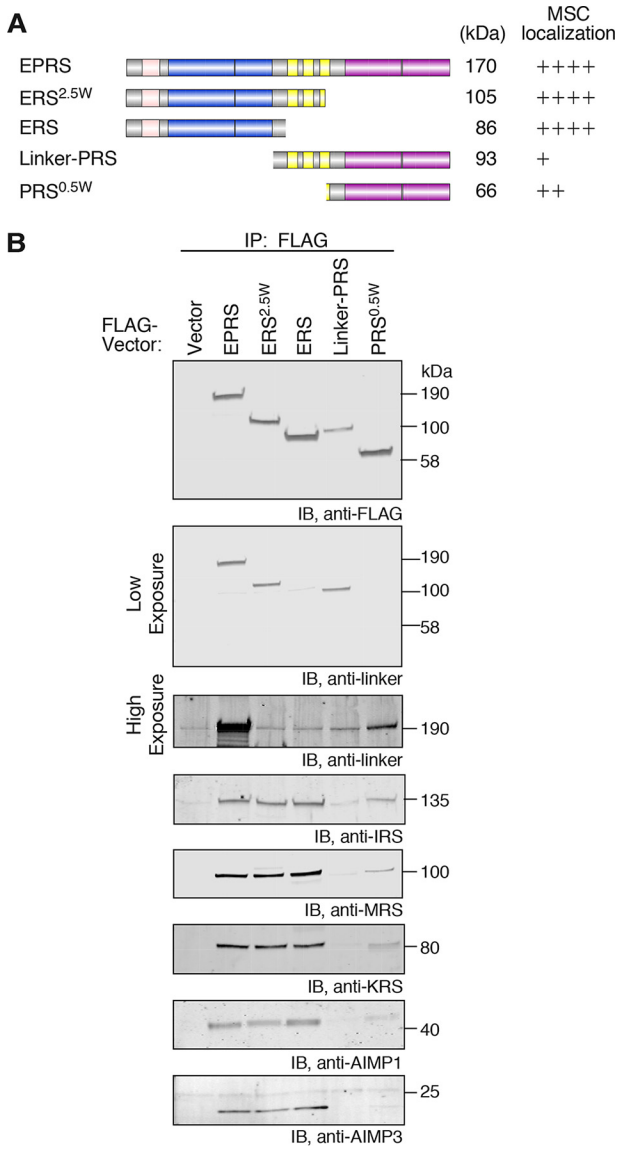

Figure 3. Interaction of caspase-generated EPRS fragments, ERS$^{2.5W}$ and PRS$^{0.5W}$, with MSC components. *A*, EPRS and truncated domains expressed in HEK293F cells with theoretical molecular mass and MSC association. *B*, immunoblot (*IB*) analysis of immunoprecipitated (*IP*) EPRS, or truncated variants, probed with antibodies for FLAG tag and MSC components.

endogenous EPRS and three MSC synthetases (IRS, MRS, and KRS) and two scaffolding proteins (AIMP1 and AIMP3), confirming its association with the MSC (Fig. 3*B*). Surprisingly, ERS$^{2.5W}$ and ERS showed weak association with endogenous EPRS but still pulled down all tested components of the MSC, including the scaffolding proteins, suggesting their ability to either displace endogenous EPRS in the MSC or to interfere with the incorporation of newly synthesized EPRS in the MSC. In contrast, PRS$^{0.5W}$ and a fragment containing the full WHEP-linker (Linker-PRS) showed comparatively weak association with both endogenous EPRS and the MSC (Fig. 3*B*). These results suggest that ERS$^{2.5W}$ associates with constituent components of the MSC, whereas PRS$^{0.5W}$ interacts indirectly through binding to endogenous EPRS within the MSC.

Apoptosis-dependent and -independent generation of ERS$^{2.5W}$ in vitro and in vivo

To detect the specific cleavage of EPRS at ^{926}DQVD^{929} *in vivo*, we took advantage of previous reports showing generation of antibodies that recognize termini newly exposed by protease cleavage (neoepitopes) but not the identical sequence in the full-length protein (35, 36). We used an octapeptide terminating with the P1 aspartate (Asp-929) to generate a polyclonal antibody for detection of ERS$^{2.5W}$ but not full-length EPRS (Fig. 1*A*). By immunoblot analysis, the neoepitope antiserum specifically recognized overexpressed ERS$^{2.5W}$ but not endogenous or overexpressed EPRS; preincubation of antiserum with immunogenic peptide markedly reduced ERS$^{2.5W}$ recognition (Fig. 4*A*, *left panel*). The comparable expression of ERS$^{2.5W}$ and endogenous EPRS was shown using anti-linker antibody (Fig. 4*A*, *right panel*). Likewise, neoepitope antiserum immunoprecipitated ERS$^{2.5W}$, but not endogenous or overexpressed EPRS, as detected by linker antibody, confirming neoepitope antibody specificity for ERS$^{2.5W}$ (Fig. 4*B*). We used the neoepitope antibody to verify generation of ERS$^{2.5W}$ from cleavage of EPRS by various caspases. Using purified FLAG-tagged EPRS (Fig. 4*C*, *left panel*), recombinant caspase-3 induced robust generation of ERS$^{2.5W}$, as well as minor fragments possibly produced by cleavage at less preferred sites within ERS (Fig. 4*C*, *right panel*). A small amount of ERS$^{2.5W}$ was generated by caspase-7. However, caspase-6 and the inflammatory caspases-1, -4, and -10 generated even less ERS$^{2.5W}$, essentially equivalent to the amount generated in the absence of added caspase, consistent

Downloaded from http://www.jbc.org/ at Rsch Cntr Julich Res library on November 22, 2018

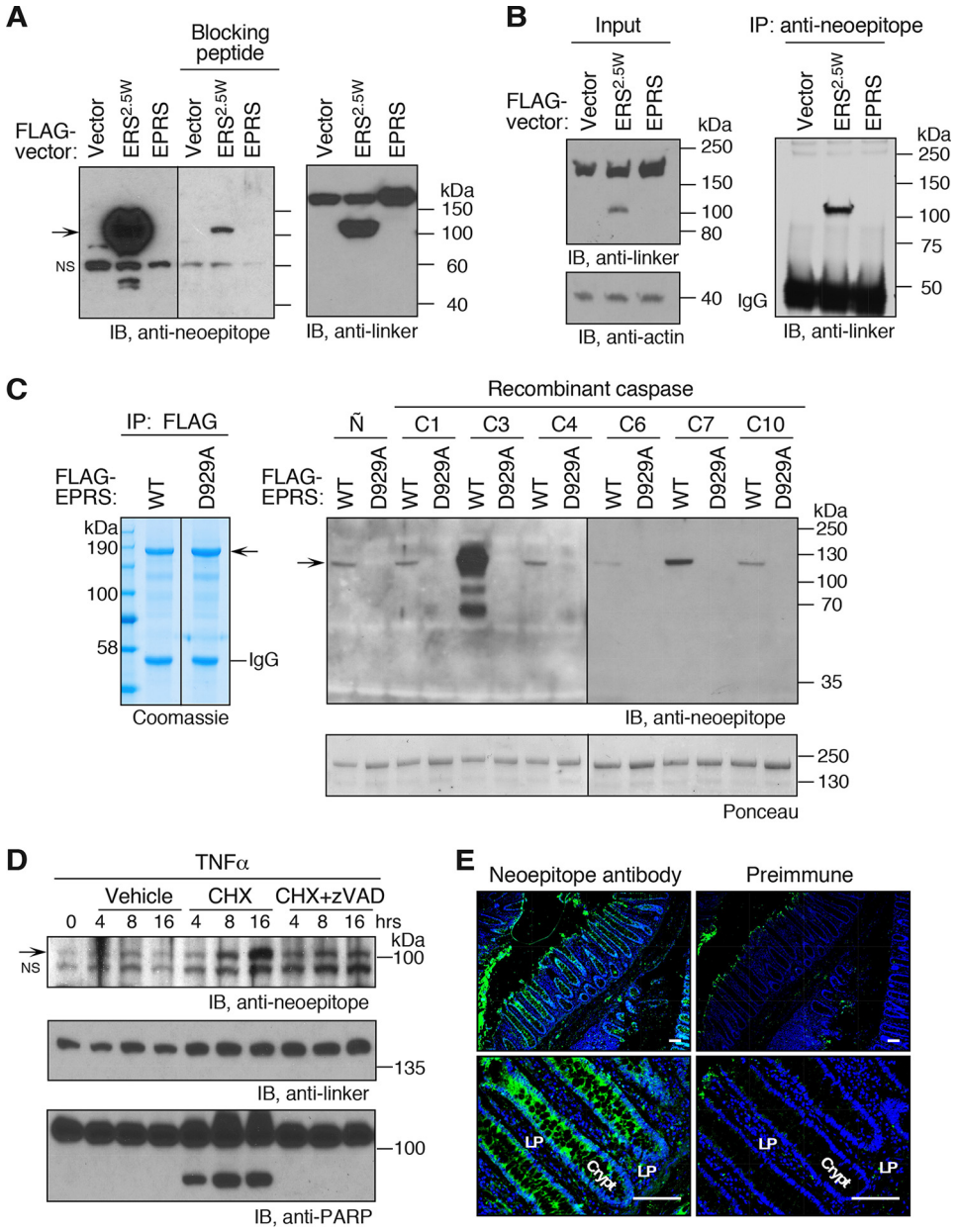

Figure 4. Detection of EPRS cleavage at Asp-929 *in vitro* and *in vivo* using neoepitope antiserum. *A,* immunoblot (*IB*) of lysates of N2a cells transfected with vector, FLAG-tagged ERS$^{2.5W}$, or full-length EPRS probed with neoepitope serum with or without blocking peptide (*left panel*) or with anti-linker antibody (*right panel*). *B,* immunoblot of lysates from HEK293F cells transfected with vector, FLAG-tagged ERS$^{2.5W}$, or EPRS before (*left panel*) or after (*right panel*) immunoprecipitation (*IP*) using neoepitope serum. *C,* Coomassie stain of FLAG-tagged EPRS purified by pulldown from HEK293F cells (*left panel*). Immunoblot of purified wildtype (WT) EPRS or D929A mutant after caspase cleavage (*right panel*). Immunoblot was Ponceau-stained and probed with neoepitope serum. *D*, immunoblot of lysates from TNFα-treated HT29 cells co-incubated with either vehicle or CHX in the presence or absence of Z-VAD (40 μM) for up to 16 h. Specific (*arrow*) and nonspecific (*NS*) immunoreactivities are indicated. *E,* immunofluorescence micrographs of human colon tissue detected with neoepitope or preimmune serum (*green*) and DAPI nuclear stain (*blue*) at 5× (*upper panel*) or 20× (*lower panel*) magnification. Lamina propria (*LP*) and colonic crypt (*crypt*) are indicated. *Scale bar* represents 100 μm.

with cleavage by an endogenous protease. Under no condition was ERS$^{2.5W}$ generated from EPRS bearing the D929A mutation.

To identify conditions that might induce ERS$^{2.5W}$ formation, the extrinsic apoptotic pathway, characterized by caspase activation following binding of extracellular ligands to cell-surface death receptors, was induced in colonic adenocarcinoma HT-29 cells by combined treatment with TNFα and cycloheximide (CHX). Caspase activation was shown by cleavage of poly(ADP-ribose) polymerase 1 (PARP1) to generate its well-characterized 89-kDa fragment in cells treated with TNFα plus CHX (Fig. 4*D*). ERS$^{2.5W}$ expression was induced by 8 h and continued to accumulate until at least 16 h. Caspase inhibition with Z-VAD inhibited PARP cleavage and ERS$^{2.5W}$ generation thereby establishing stimulus-dependent generation of ERS$^{2.5W}$ by caspase-mediated cleavage of endogenous substrate. Because enterocyte turnover in the colon upper crypt depends on caspase activity (37–39), we investigated ERS$^{2.5W}$ generation in human colon. Strong ERS$^{2.5W}$ immunoreactivity was observed near the top of the crypt, gradually attenuating

Downloaded from http://www.jbc.org/ at Rsch Cntr Julich Res library on November 22, 2018

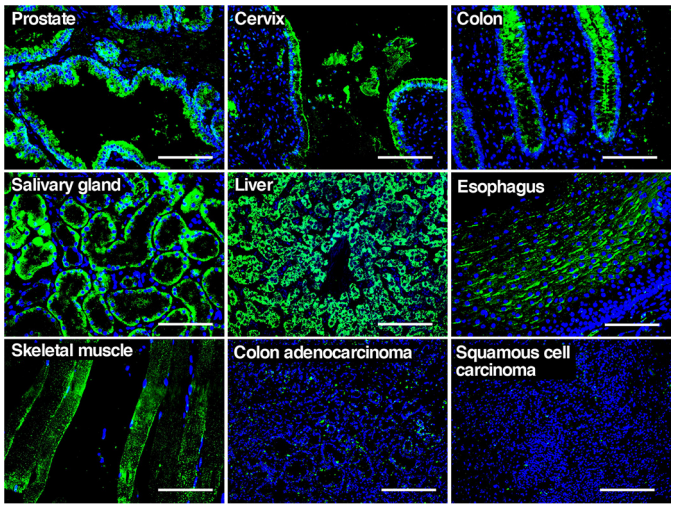

Figure 5. *In vivo* detection of ERS$^{2.5W}$. Immunofluorescence micrographs of human tissue microarray detected with neoepitope serum (*green*) and DAPI (*blue*) are shown. *Scale bars* represent 100 μm.

toward the proliferative region at the crypt bottom where caspase activity is low (Fig. 4*E*). These results provide *in vivo* evidence for ERS$^{2.5W}$ generation in the context of enterocyte apoptosis, particularly during enterocyte turnover in the normal colonic crypt.

We investigated *in vivo* expression of ERS$^{2.5W}$ in a panel of human tissues. ERS$^{2.5W}$ was detected in epithelial cells of the prostate, cervix, and colon, as well as in acinar cells of the salivary gland (Fig. 5). ERS$^{2.5W}$ was robustly expressed in hepatocytes, squamous epithelial cells of the esophagus, where it was present primarily on the apical aspect, and in skeletal muscle. Interestingly, ERS$^{2.5W}$ expression was undetectable in squamous cell carcinoma and advanced-stage colonic adenocarcinoma. These results indicate that EPRS cleavage occurs in multiple healthy human tissues *in vivo*.

Solution structure of ERS$^{2.5W}$ and ERS by small-angle neutron scattering (SANS)

With the identification of ERS$^{2.5W}$ as a new EPRS proteoform, we next characterized the structural consequences of WHEP domain fusion to the C terminus of the catalytic core of the glutamyl-tRNA synthetase. SANS can reveal the size, shape, and conformation of macromolecules in solution under near-physiological conditions and was used to investigate the structures of recombinant ERS$^{2.5W}$ and the ERS variant lacking the entire linker region. Because SANS structural analysis requires highly homogeneous protein preparations of single-particle species, ERS$^{2.5W}$ and ERS protein preparations were purified in two steps: His-tag nickel affinity purification followed by size-exclusion chromatography (SEC). A single peak fraction was collected and characterized again directly prior to SANS measurements by SEC and amine-specific cross-linking. SEC revealed near-homogeneous preparations with predominantly monomeric peaks for ERS$^{2.5W}$ (peak III) and ERS (peak V) (Fig. 6*A* and Table 1). Minor fractions of apparent trimers for ERS$^{2.5W}$ (peak II) or dimers for ERS (peak IV) were observed. Some aggregation was consistently observed in ERS$^{2.5W}$ preparations, and because it was not removed by SEC, it might reflect a state of equilibrium. Interestingly, the apparent 124-kDa molecular mass of ERS$^{2.5W}$ was larger than the expected 105 kDa, whereas the apparent 60-kDa molecular mass of ERS was smaller than the expected 86 kDa (Table 1). Amine-specific cross-linking with bissulfosuccinimidyl suberate (BS3) confirmed the predominant monomeric state of ERS$^{2.5W}$ and ERS, as well as small amounts of putative trimers and dimers, respectively; the diffuse bands in the presence of BS3 might be caused by variable cross-linking to free lysines (Fig. 6*B*).

We next collected the SANS scattering intensities of ERS$^{2.5W}$ and ERS at very small angles (Fig. 6*C*). Guinier approximation plots, which give an estimate of particle dimension, confirmed sample homogeneity and absence of substantial aggregation in both ERS$^{2.5W}$ and the ERS preparations (Fig. 6*D*). Because of the presence of a small amount of aggregates in the ERS$^{2.5W}$ sample analyzed by SANS (Fig. 6*A*, less than 5%), we evaluated the stability of the $P(r)$ function (the change in function's profile) in the presence and absence of the aggregates. The aggregates produced three intensity points at a low-scattering angle that do not obey Guinier linearity (Fig. S1*A*). Removal of these nonlinear points from the scattering intensity curve at zero angle and deconvolution of the trimmed intensity curve obtained highly similar $P(r)$ function to the one corresponding to a sample without aggregates (Fig. S1*B*). Similarly, exclusion of nonlinear points resulted in less than 2% reduction in the computed scattering intensity and radius of gyration measurements (Table S1). These results indicate that the low amount of aggregation observed in the ERS$^{2.5W}$ sample preparation had little effect on the overall shape of the $P(r)$ function and the magnitude of the radius of gyration in this analysis.

The radius of gyration was calculated to be 63 Å for ERS$^{2.5W}$ and 48.7 Å for ERS (Table 2). Kratky plots, in which curve shape reports the degree of globularity and flexibility of polymer chain conformation, displayed distinct, interference-free SANS profiles for ERS$^{2.5W}$ and ERS, characteristic of flexible multidomain particles (Fig. 6*E*) (40). Overlay of Kratky plots and derived pair-distance distribution functions ($P(r)$) for ERS$^{2.5W}$ and ERS clearly show substantial differences in the conformational state of the proteins (Fig. 6, *E* and *F*).

The SANS data were subjected to *ab initio* computational modeling with DAMMIN software, which uses simulated plausible conformers that best agree with the experimental scattering curves at 20-Å resolution (41). Using minimal ensemble search, final average shapes representing the common features of 16 individual conforms were derived for ERS$^{2.5W}$ and ERS (Fig. 7, *A* and *B*). ERS$^{2.5W}$ displays an elongated, bent structure with maximum vertical and horizontal particle dimensions of 170 and 79 Å, respectively (Fig. 7*A*). In contrast, ERS has globular features with N- and C-terminal curvatures and maximum vertical and horizontal dimensions of 140 and 69 Å, respectively (Fig. 7*B*). Superimposition of the two structures in two alternative orientations highlighted these shape variations (Fig. 7, *C* and *D*) and suggested global conformational changes in the catalytic core imposed by the appended WHEP domains. To validate the conformational variations observed in the SANS analysis, we took advantage of the fact that ERS$^{2.5W}$ and ERS share a total of 15 tryptophan residues, which localize strictly within the GST–C domain and the catalytic core and are absent from

Downloaded from http://www.jbc.org/ at Rsch Cntr Julich Res library on November 22, 2018

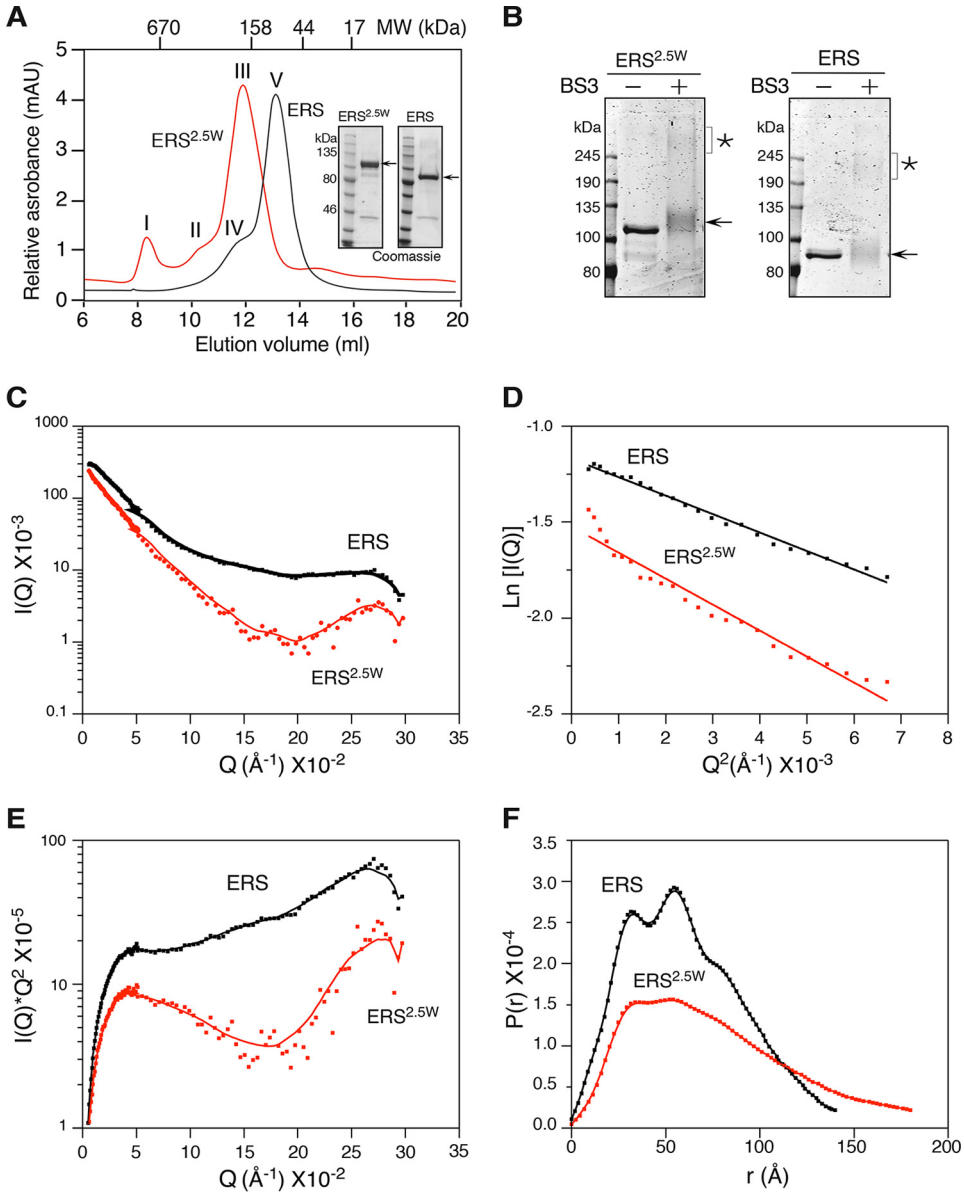

Figure 6. Solution structures of ERS$^{2.5W}$ and ERS in the ligand-free state as determined by SANS. *A*, size-exclusion chromatography of recombinant ERS$^{2.5W}$ (*red*) and ERS (*black*). Molecular mass standards are indicated on *top*. Coomassie-stained gel of purified recombinant ERS$^{2.5W}$ and ERS (*insets*). *B*, Coomassie stain analysis of recombinant ERS$^{2.5W}$ (*left panel*) and ERS (*right panel*) before and after BS^3 cross-linking; monomer (*arrow*) and oligomer (*) species are indicated. *C*, scattering intensity (*I*) as a function of scattering vector (*Q*) for ERS$^{2.5W}$ (*red*) and ERS (*black*). *D*, Guinier plot of ERS$^{2.5W}$ (*red*) and ERS (*black*). *E*, overlay of Kratky plots of scattering data comparing ERS$^{2.5W}$ (*red*) and ERS (*black*) showing altered domain structure. *F*, overlay of pair-distance distribution function, *P*(*r*), of ERS$^{2.5W}$ (*red*) and ERS (*black*) showing distinct conformational features.

Table 1

Molecular mass analysis of purified recombinant ERS$^{2.5W}$ and ERS by size-exclusion chromatography

Calc. indicates calculated and Pred. indicate predicted.

Elution peak	Elution volume	Molecular mass$_{Calc.}$	Observed oligomeric state	Molecular mass$_{Pred.}$
	ml	*kDa*		*kDa*
ERS$^{2.5W}$				105
I	8.47(void)	>600	Aggregates	ND[a]
II	10.40	311	Trimer	315
III	11.97	124	Monomer	105
ERS				86
IV	12.06	118	Dimer	172
V	13.21	60	Monomer	86

[a] ND means not determined (outside resolution range).

the appended 2.5W WHEP-linker domains (Fig. 8*A*). Therefore, any changes in the intrinsic tryptophan fluorescence of the protein will necessarily reflect changes in the folding state of the catalytic core and/or the GST–C domain. Analysis of intrinsic tryptophan fluorescence showed significantly reduced fluorescence for ERS$^{2.5W}$ (548.3 ± 3.4) compared with ERS (606.2 ± 10.9), although both fluorescence spectra peaked at a wavelength of 341 nm (Fig. 8, *B* and *C*). These data suggest localized quenching of tryptophan residues within the structure of ERS$^{2.5W}$ compared with ERS. Next, we probed the protein-folding state using the limited proteolysis assay and antibodies specific for the N-terminal His-tag (Fig. 8, *A* and *D*, *green*) or the catalytic core (Fig. 8, *A* and *D*, *red*). Full-length ERS$^{2.5W}$ dis-

Downloaded from http://www.jbc.org/ at Rsch Cntr Julich Res library on November 22, 2018

Table 2
Ligand-induced changes in the properties of recombinant ERS$^{2.5W}$ and ERS in solution

	Normalized SANS[a]		Gyration radius[b]		Maximal dimension[c]	
	Ligand-free	Ligand-occupied	Ligand-free	Ligand-occupied	Ligand-free	Ligand-occupied
	$(cm^{-1})/\mu g$		Å		Å	
ERS$^{2.5W}$	6.7×10^{-4}	1.3×10^{-3}	63	83.6	180	220
ERS	4.8×10^{-4}	7.3×10^{-4}	48.7	64	140	180

[a] Experimentally determined SANS intensity normalized to protein concentration.
[b] Gyration radius determined by Guinier approximate analysis.
[c] Maximal dimension derived from the pair-distance distribution function.

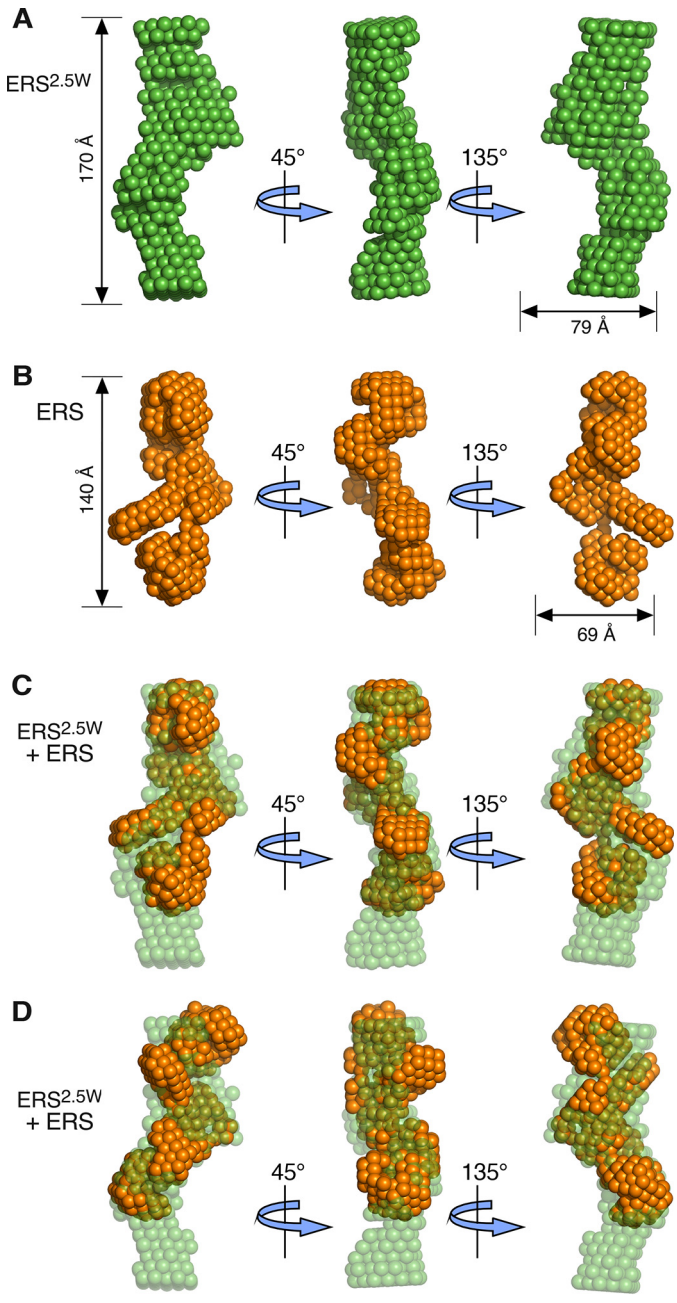

Figure 7. *Ab initio* modeling of WHEP-dependent conformational rearrangement of the catalytic core and appended GST–C domain. *A–D*, conformers of ERS$^{2.5W}$ (*A, green*), ERS (*B, orange*), and overlays (*C* and *D*) constructed from minimal ensemble search of 16 possible conformers derived using DAMMIN *ab initio* modeling of SANS data. Three rotational displays are visualized using PyMOL. Measurements of maximal vertical and horizontal dimensions are indicated by *double-headed arrows*.

played increased N-terminal susceptibility to proteolysis compared with full-length ERS as detected by the His-tag antibody (Fig. 8, *D* and *E*, compare *FL* and *F3* in *D, upper* and *lower left panels*). Similarly, the catalytic core of full-length ERS$^{2.5W}$ showed not only increased susceptibility to proteolysis compared with ERS but also a different proteolysis pattern (Fig. 8, *D* and *F*, compare *F1* and *F2* fragments in *D, upper* and *lower middle panels*). Together, these data support the existence of conformational differences in the folding state of the N-terminal GST–C domain and the synthetase core imposed by the C-terminally appended 2.5W WHEP-linker.

Substrate-dependent self-association of ERS is regulated by WHEP domains

We used SANS to investigate conformational changes in ERS and ERS$^{2.5W}$ induced by substrate binding. The scattering intensities were compared in the presence of ERS substrates, ATP and L-glutamate (Table 2). We observed an increase in the scattering intensity of both ERS$^{2.5W}$ and ERS, compared with the free states (Table 2). The Guinier plots showed overall linear profiles for ERS$^{2.5W}$ and ERS, ruling out nonspecific aggregation (Fig. 9, *A* and *B*). The minor aggregation observed in the ERS$^{2.5W}$ sample preparation resulted in two nonlinear points in the Guinier plot at low angle (Fig. 2*A*). Removal of these nonlinear points had little effect on the $P(r)$ function (Fig. S2*B*) and resulted in less than 2.2% reduction in the computed scattering intensity and radius of gyration (Table S2). The radius of gyration was calculated at 83.6 Å for ERS$^{2.5W}$ and 64.0 Å for ERS, representing an increase of 20.6 and 15.3 Å relative to the unbound states, respectively (Table 2). Kratky plot analysis revealed that substrate binding induced a large conformational change in ERS$^{2.5W}$ compared with ERS, consistent with an increase in flexibility and a reduction in globular domain arrangement (Fig. 9*C*). The computed pair-distance distribution function revealed a maximal dimension of 220 Å for ERS$^{2.5W}$ and 180 Å for ERS in the occupied states, which represented an increase of 40 Å for each protein variant relative to free states (Fig. 9*D*, Table 2). Together, for both ERS$^{2.5W}$ and ERS, the ligand-dependent increase in the radius of gyration and the corresponding increase in the calculated particle dimension suggest formation of larger protein complexes through self-association.

To determine whether ligand binding induced self-association of ERS$^{2.5W}$ and ERS, microscale thermophoresis was used to quantify protein–protein interactions. Fluorescently-labeled ERS$^{2.5W}$ and ERS were first pre-incubated with ligands (ATP and L-Glu) to initiate self-association. Unlabeled protein was

Downloaded from http://www.jbc.org/ at Rsch Cntr Julich Res library on November 22, 2018

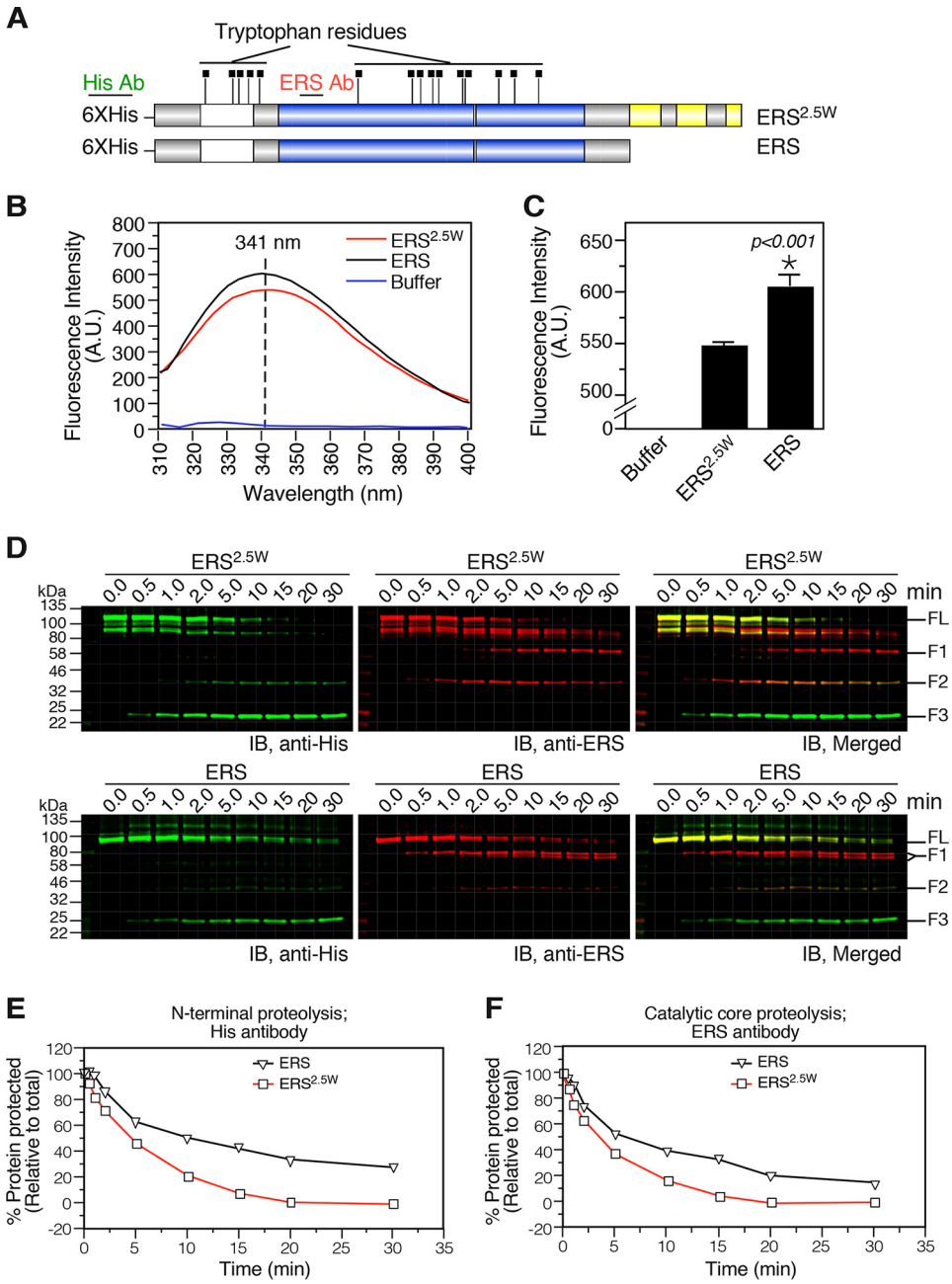

Figure 8. Appended WHEP domains alter the conformational state of the synthetase core and appended GST–C domain. *A,* ERS$^{2.5W}$ and ERS domain organization with indicated localization of tryptophan residues and antibody-binding epitopes. *B,* spectra of intrinsic protein fluorescence of ERS$^{2.5W}$, ERS, or buffer only with peak fluorescence wavelength indicated at 341 nm. *C,* quantification of peak intrinsic fluorescence of ERS$^{2.5W}$, ERS, or buffer only from triplicate measurements ± S.D. *Asterisk* indicates statistical significance at $p < 0.001$. *D,* quantitative Western blotting of ERS$^{2.5W}$ (*upper panel*) or ERS (*lower panel*) subjected to trypsin digestion for the indicated times using antibodies directed against the His-tag (*green*) or the ERS domain (*red*). Overlay of the *green* and *red* immunoblots (*IB*) (*merged*) identifies protein fragments with dual immunoreactivity for the His-tag and ERS domain antibodies (*yellow*). *E* and *F,* quantification of full-length protein remaining after trypsin digestion at the indicated time points as detected by the His epitope antibody (*E*) or ERS domain antibody (*F*) for ERS$^{2.5W}$ (*red*) or ERS (*black*). *A.U.,* arbitrary units.

then titrated to measure the dissociation constant (K_D), defined as the concentration of unlabeled protein required to displace the intermolecular interactions of the fluorescently labeled protein (Fig. 10*A*). Parallel measurements were performed in the absence of ligand, where self-association is expected to be minimal. Therefore, a higher interaction K_D would indicate prior self-association state of the labeled protein.

As a quality control test, both ERS$^{2.5W}$ and ERS displayed at least 5 amplitude units of change in normalized fluorescence intensity (ΔFnorm) when exposed to increasing concentrations of unlabeled proteins under all conditions tested (Fig. 10, *B* and *D*). In the ligand-free state, ERS$^{2.5W}$ bound its unlabeled counterpart with an affinity of 4.32 μM compared with 0.046 μM for ERS (Fig. 10, *B* and *D*; Table 3), and 74% of fluorescently-labeled ERS$^{2.5W}$ associated with its unlabeled variant compared with 99.5% for ERS (Fig. 10, *C* and *E*, and Table 3). These results suggest that a relatively larger pool of ERS$^{2.5W}$ (~26%) already existed in a stable self-associated state compared with ERS

Downloaded from http://www.jbc.org/ at Rsch Cntr Julich Res library on November 22, 2018

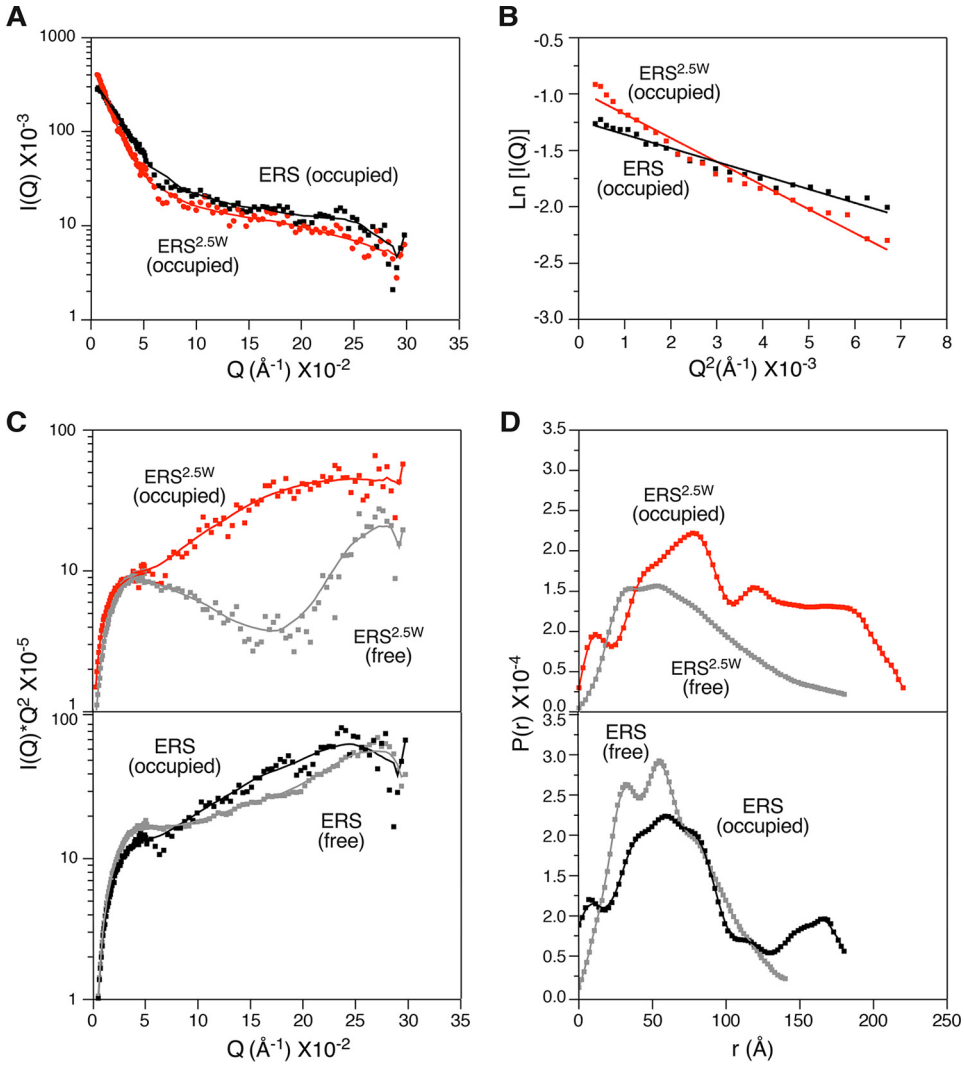

Figure 9. Ligand-dependent conformational changes in ERS$^{2.5W}$ and ERS determined by SANS. *A,* scattering intensity as a function of scattering vector (*Q*) for ERS$^{2.5W}$ (*red*) and ERS (*black*) in the presence of ligands. *B,* Guinier plots of ERS$^{2.5W}$ (*red*) and ERS (*black*) in the presence of ligands. *C,* overlay of Kratky plots of scattering data showing changes in the conformational state of ERS$^{2.5W}$ (*top panel*) or ERS (*bottom panel*) in response to ligand binding. *D,* overlay of pair-distance distribution function, *P*(*r*), showing changes in the conformational state of ERS$^{2.5W}$ (*top*) or ERS (*bottom*) in response to ligand binding. *Red* and *black traces* indicate ERS$^{2.5W}$ and ERS, respectively, in ligand-occupied states (*occupied*); *gray traces* show ligand-free states (*free*) of both proteins.

(~0.5%), thus leading to about a 100-fold increase in dissociation constant compared with ERS. Ligand binding increased the dissociation constant of both ERS$^{2.5W}$ and ERS, indicating self-association of both protein variants (Table 3). ERS$^{2.5W}$ displayed a dissociation constant of 26 μM compared with 5.33 μM for ERS, representing a 5-fold increase compared with ERS (Fig. 10, *B* and *D*; Table 3). The maximal self-association of ERS$^{2.5W}$ and ERS in the presence of ligand was estimated at 65 and 36%, respectively (Fig. 10, *C* and *E*; Table 3). Because the difference in the observed maximal self-association between ERS$^{2.5W}$ and ERS can be attributed to the ligand-free self-association of ERS$^{2.5W}$, we tested whether ERS$^{2.5W}$ co-purified with ligands. Indeed, in a pyrophosphate-ATP exchange assay, ERS$^{2.5W}$, but not ERS, displayed enzymatic activity and generated ATP from pyrophosphate without exogenous ATP and in a tRNA-dependent manner (Fig. S3). Furthermore, binding affinities for ATP, tRNA, and L-glutamate were determined by MST (Fig. 10*F*; Table 4). ERS$^{2.5W}$ displayed ~2.5-fold greater affinity for ATP and tRNA, but showed no difference in the binding affinity to L-glutamate (Table 4). Collectively, these results indicate ligand binding induces self-association of ERS$^{2.5W}$ independent of the WHEP domains, but that WHEP domains promote self-association by enhancing the affinity for ligand binding and stabilizing this interaction.

We investigated whether the self-association capabilities of ERS$^{2.5W}$ and ERS in solution might explain the changes in the SANS intensities observed upon substrate binding. Our results show small pools of ERS$^{2.5W}$ and ERS as trimers and dimers in solution, respectively (Fig. 6, *A* and *B*; Table 1). These oligomerization states, and their abundance in the presence and absence of ligands as inferred by MST, were used to compute the theoretical SANS intensities by SANScript and test how closely it matched the measured SANS intensities (Table 5). In the ligand-free state, the calculated intensity for ERS$^{2.5W}$ differed from the measured value by only about 20%. For ERS, the intensity calculated with SANScript differed from the measured value by 3%. For both variants, the measured and calculated SANS intensities were consistent with predominantly mono-

Downloaded from http://www.jbc.org/ at Rsch Cntr Julich Res library on November 22, 2018

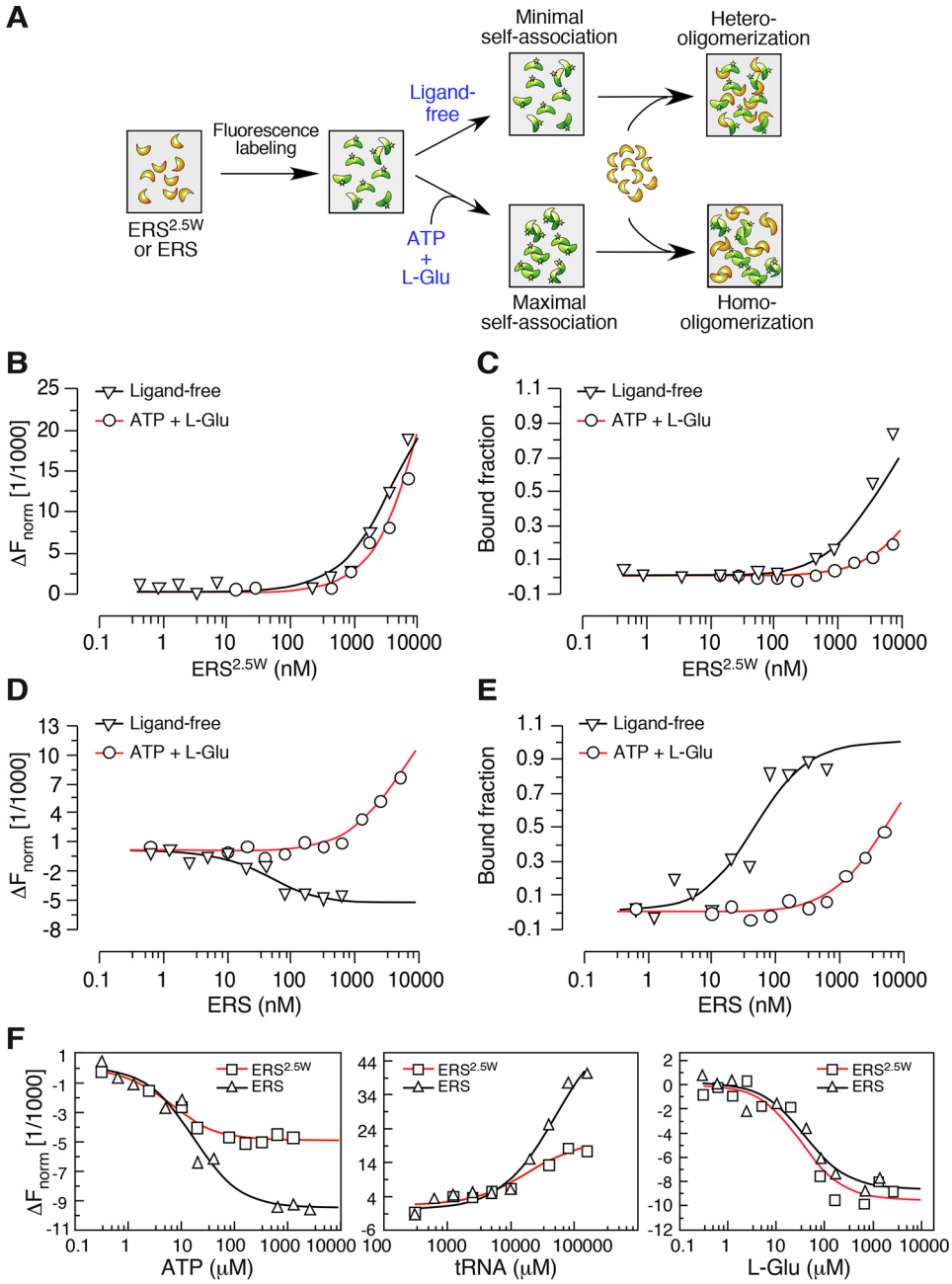

Figure 10. WHEP domains facilitate ERS$^{2.5W}$ self-association in response to ligand binding. *A,* schematic of MST experimental design. Fluorescently-labeled protein remains monomeric in the absence of ligand and self-associates in the presence of ligands (*ATP + L-Glu*). Titration of unlabeled protein in MST results in binding and formation of labeled/unlabeled hetero-oligomers. Ligand-induced self-association impedes hetero-oligomerization, resulting in an apparent higher dissociation constant (K_D) and a smaller fraction of bound labeled protein. *B* and *D,* change in thermophoretic mobility of labeled ERS$^{2.5W}$ (*B*) or ERS (*D*) in response to titration of unlabeled protein. *C* and *E,* fraction of bound labeled ERS$^{2.5W}$ (*C*) or ERS (*E*) as a function of unlabeled protein titration. *F,* change in MST-determined thermophoretic mobility of labeled ERS$^{2.5W}$ (*red*) and ERS (*black*) in response to ATP, tRNA, or L-Glu.

Table 3
Effect of ligand binding on the self-association of ERS$^{2.5W}$ and ERS as analyzed by MST

	Ligand-free			Ligand-occupied		
	Interaction K_D	Maximum bound (labeled)	Inferred self-association (labeled)	Interaction K_D	Maximum bound (labeled)	Inferred self-association (labeled)
	μM	%	%	μM	%	%
ERS$^{2.5W}$	4.320 ± 1.10	74.0	26.0	26.0 ± 12.1	35.0	65.0
ERS	0.046 ± 0.03	99.5	0.50	5.33 ± 2.91	63.6	36.4

Downloaded from http://www.jbc.org/ at Rsch Cntr Julich Res library on November 22, 2018

Table 4
Substrate-binding affinities of ERS$^{2.5W}$ and ERS as determined by MST

	ATP K_D	tRNA K_D	L-Glu K_D
	μM	μM	μM
ERS$^{2.5W}$	6.30 ± 1.8	19.0 ± 9.00	33.1 ± 16.0
ERS	16.8 ± 4.9	52.0 ± 16.5	38.0 ± 14.7

Table 5
Comparison of MST and SANScript-predicted oligomeric state distribution for ERS$^{2.5W}$ and ERS

	Normalized SANS intensity (cm^{-1})/μg			
	Ligand-free		Ligand-occupied	
	SANScript calculated	Experimentally measured	SANScript calculated	Experimentally measured
ERS$^{2.5W}$	8.3×10^{-4}	6.7×10^{-4}	1.3×10^{-3}	1.3×10^{-3}
ERS	4.7×10^{-4}	4.8×10^{-4}	6.3×10^{-4}	7.3×10^{-4}

disperse populations (Table 5). In the presence of ligand, the calculated and measured SANS intensities were essentially identical for ERS$^{2.5W}$. For ERS, the calculated intensity differed from the measured value by about 14%. Altogether, the concordance of the SANScript-calculated and measured SANS intensities supports the enhanced tendency of ERS$^{2.5W}$ to form oligomers in solution, as well as the differential oligomeric state of ERS$^{2.5W}$ and ERS upon ligand binding.

Discussion

Noncatalytic domains in eukaryotic tRNA synthetases are associated with functional diversity and serve as regulators of canonical (18, 42–44) and noncanonical activities (45). The WHEP domain is a synthetase-specific noncatalytic domain that functions as an atypical RNA- and protein-binding domain in EPRS (7, 46). In this study, we demonstrate that the third WHEP domain of EPRS contains a highly conserved caspase-cleavage site, ^{926}DQVD^{929}, which bisects the protein into two intact synthetase fragments, ERS$^{2.5W}$ and PRS$^{0.5W}$. With the remarkable selectivity of caspases for the ^{926}DQVD^{929} cleavage site in EPRS, and with the striking conservation of this sequence across more than 600 million years of evolution, it is likely that it is a functionally significant cleavage event. Fragments of EPRS can be generated by additional post-transcriptional and post-translational mechanisms, such as coding-region polyadenylation (EPRS-N1) (14) and calpain-mediated cleavage (30). EPRS-N1 is basally produced in several cell types and is a competitive inhibitor of GAIT complex assembly on target mRNA during translational repression (14). Calcium-activated calpains target EPRS at several undefined sites, including the WHEP linker, and it is unclear whether calpain-generated EPRS fragments are proteolytically stable *in vivo* (30). In contrast, caspase-3 and -7 are activated via regulated intrinsic and extrinsic pathways in apoptotic and nonapoptotic contexts and proteolytically process highly specific consensus sites, often generating bioactive fragments (47). Here, we show that the caspase-derived EPRS fragment, PRS$^{0.5W}$, retained limited catalytic activity *in vitro* with the latter supported by recent studies on the structure and activity of the isolated PRS domain of EPRS (residues 1016–1512) (48). This contrasts to the weak activity measured for ERS$^{2.5W}$ under the conditions used. Our results do not exclude the possibility that caspase cleavage of EPRS may be required for inactivation of an undiscovered noncanonical function or for the generation of bioactive fragments with unique noncanonical activities. Nonetheless, the identification of the ERS$^{2.5W}$ fragment in normal tissue provides a unique opportunity to study the glutamyl-tRNA synthetase in the context of its appended noncatalytic domains.

ERS$^{2.5W}$ comprises the glutamyl-tRNA synthetase with an N-terminally appended GST–C domain and two complete and one partial WHEP domain at the C terminus. Each WHEP domain is composed of 46 amino acids adapting a helix-turn-helix structure. Here, we show that the WHEP domains have no apparent role in mediating ERS association with the MSC. Among the WHEP-containing synthetases (WRS, HRS, EPRS, MRS, and GRS), only EPRS and MRS are present in the MSC. In current models of MSC assembly, both EPRS and MRS engage the MSC through N-terminally appended GST–C domains, which are lacking in WHEP-containing synthetases not in the MSC (24, 49), suggesting that the WHEP domain is not sufficient to confer MSC localization. In agreement with this model, our results indicate that ERS$^{2.5W}$ and ERS localize to the MSC through GST–C domain interactions and that the WHEP domains are dispensable for MSC localization. Other studies indicated a role for the EPRS WHEP domains in binding to IRS and RRS in the MSC (50, 51) and showed diminished IRS and RRS expression in the absence of EPRS (52). Our results show association of IRS with the MSC in the presence of EPRS, ERS$^{2.5W}$, or WHEP domain–deleted mutant ERS. Although we cannot rule out a secondary role for EPRS WHEP domains in binding to IRS within the MSC, our results are consistent with an important role of GST–C domain interactions as the primary determinant of IRS localization and stability in the MSC.

Overall, our SANS structural analysis suggests a role for the WHEP domains in promoting an accessible and elongated arrangement of its associated glutamyl-tRNA synthetase. However, one limitation of SANS analysis is that the structures computed by *ab initio* modeling represent an average shape of 16 plausible structures, rather than the absolute shape of the protein. Also, minor protein aggregation or multimerization can potentially confound the data and alter the derived structures. Therefore, conformational differences observed by SANS should be validated using biochemical and biophysical approaches. In support of the structural differences observed by SANS, ERS$^{2.5W}$ and ERS displayed distinct hydrodynamic properties by SEC, differences in domain susceptibility to proteolysis, and distinct intrinsic protein fluorescence profiles. Consistent with its elongated and noncompact nature, SEC analysis showed an apparent molecular mass of ERS$^{2.5W}$ that is larger than expected. ERS$^{2.5W}$ displayed greater susceptibility to proteolytic processing and lower total intrinsic protein fluorescence compared with the ERS variant lacking the WHEP domains. Furthermore, our nonlinear Guinier point exclusion analysis clearly demonstrates that the minor aggregation observed in ERS$^{2.5W}$ protein preparation had little effect on the SANS-derived structures. Interestingly, the overall SANS structure of ERS$^{2.5W}$ is reminiscent of the small-angle X-ray scattering-derived structure of the MSC (53), which exhibited an elongated and multiarmed shape, with demonstrated in-

Downloaded from http://www.jbc.org/ at Rsch Cntr Julich Res library on November 22, 2018

creased surface accessibility to proteases such as caspases (31) and calpains (30). One implication of this finding is that the WHEP domains of EPRS may contribute in part to the hydrodynamic shape of the MSC. Furthermore, such accessibility may be necessary for promoting EPRS phosphorylation and its stimulus-dependent release from the MSC (26, 29).

In addition to controlling the overall shape of the protein, our study presents several indications that the WHEP domains may influence the interaction interphase of the GST–C domain. By utilizing ERS as a biochemical tool to analyze the structural effects of the evolutionarily conserved fusion of WHEP domains to the C terminus of ERS, we demonstrated that ligand binding induced differential oligomerization states for ERS$^{2.5W}$ and ERS, with ERS$^{2.5W}$ preferentially forming trimers and ERS forming dimers. These oligomerization states were observed, in low abundance, in the absence of ligands by chemical cross-linking and size-exclusion analysis and were corroborated, in the presence of ligand, by SANScript computational analysis. These distinct oligomeric states are consistent with a role for the WHEP domains in influencing the conformation of the GST–C domain, which can form a maximal oligomerization state of tetramers (49). The role of the WHEP linker in influencing GST–C domain interactions may, in part, explain how phospho-sites within the linker may signal stimulus-dependent mobilization of EPRS from the MSC (26, 29). Although the conformational differences observed in the GST–C domain region did not influence interactions with the MSC, our results cannot exclude the possibility that these differences may influence the affinity or the regulation of these interactions.

The precise molecular mechanism driving ligand-induced self-association of the glutamyl-tRNA synthetase remains unclear; nonetheless, our data indicate it does not require the WHEP domains and thus might involve intramolecular communication between the catalytic domain and the N-terminal GST–C domain. However, the WHEP domains in ERS$^{2.5W}$ have a modulatory influence on oligomerization as they promote trimerization *versus* dimerization and increase the affinity for self-association. The latter might depend on the enhanced binding affinity for ATP in ERS$^{2.5W}$ compared with ERS. Interestingly, dimerization of glutamyl-tRNA synthetase from wheat germ has been described and shown to be essential for catalytic activity (54, 55). At an estimated molecular mass of 83 kDa (54), the wheat germ glutamyl-tRNA synthetase might indeed contain a dimerization-promoting GST–C domain.

Supporting a broader role for WHEP domains in conformational regulation of tRNA synthetases, the WHEP domain of GRS in *C. elegans* is implicated in control of its dynamic structure and aminoacylation activity (43). Furthermore, pathogenic mutations in GRS that alter the dimer interface (56) result in WHEP-dependent ectopic accumulation of the protein at motor neuron presynaptic junctions through induction of a cytotoxic "neomorphic" conformation (20). The WHEP motif is also present as a single-copy motif in WRS, where it acts on endothelial cells as a negative regulator of angiostatic activity (57). Deletion of the WRS WHEP domain, by proteolytic processing (58) or by alternative splicing (12), leads to ectopic interaction of the active site with tryptophan residues on vascular endothelial-cadherins (16), consistent with a role for the

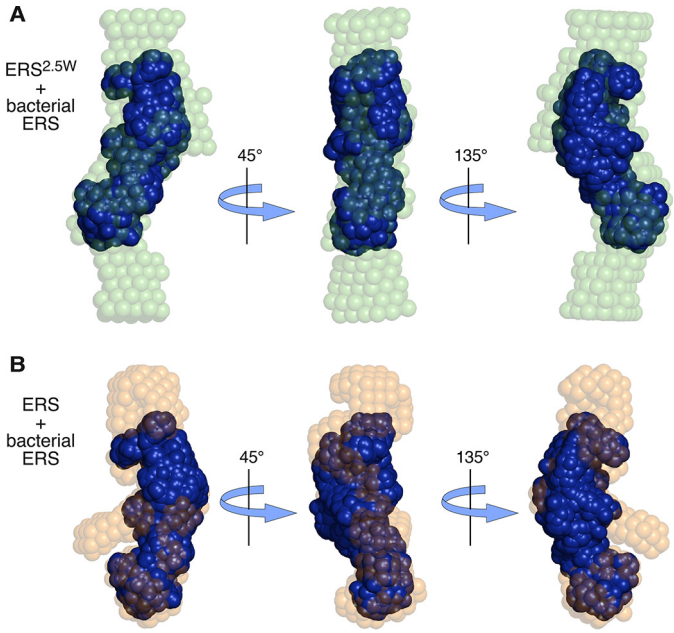

Figure 11. Structural arrangement of the glutamyl-tRNA synthetase as a bent rod is a shared feature of prokaryotic and eukaryotic synthetases. *A* and *B*, superposition of the surface structure of *Thermus thermophilus* ERS (*blue*) on SANS-derived structures of human ERS$^{2.5W}$ (*green*) (*A*) and ERS (*orange*) (*B*) in three rotational displays as visualized by PyMOL.

WHEP domains in long-distance regulation of WRS conformation. These studies, together with our structural and biochemical characterization of ERS$^{2.5W}$, suggest a broader role for the WHEP domain in controlling the global conformational state of its host tRNA synthetases, with biochemical consequences that may vary for distinct tRNA synthetases.

In summary, our analysis of ERS$^{2.5W}$ provides the first structural clues on the eukaryotic glutamyl-tRNA synthetase and its appended noncatalytic domains. Strikingly, despite the presence of appended noncatalytic domains, ERS$^{2.5W}$ and ERS share the bent-rod structural arrangement with their bacterial homologue (Fig. 11) (59). Future studies at or near the atomic resolution level, by X-ray crystallography or cryo-EM, will help to decipher the nature of the conformational changes induced by the WHEP domains and how they may relate to the overall shape and assembly of the MSC.

Experimental procedures

Cell culture, reagents, and antibodies

HEK293F cells were purchased from Thermo Fisher Scientific (Waltham, MA). Mouse brain neuroblastoma Neuro-2a (N2a), and human colon adenocarcinoma (HT-29) cell lines were purchased from ATCC (Manassas, VA). All cells were cultured in high-glucose Dulbecco's modified Eagle's medium supplemented with 10% fetal bovine serum (FBS) and 4 mM L-glutamine, except for HT-29 that was cultured in McCoy's 5A media supplemented with 10% FBS and 4 mM L-glutamine. Pan-caspase inhibitor, Z-VAD-FMK, and protein synthesis inhibitor, cycloheximide, were purchased from Enzo Life Sciences (Farmingdale, NY) and Sigma, respectively. Polyethyleneimine transfection reagent was obtained from Polysciences (Warrington, PA). Monoclonal FLAG peptide and His-tag antibod-

Downloaded from http://www.jbc.org/ at Rsch Cntr Julich Res library on November 22, 2018

ies were purchased from Sigma and Genscript (Piscataway, NJ), respectively. EPRS linker antibody was raised in the laboratory as described previously (7). Rabbit EPRS antibodies directed against the ERS or PRS domains were purchased from EPITOMICS (Burlingame, CA) and Bethyl (Montgomery, TX), respectively. Mouse mAb targeting the PRS domain of EPRS was purchased from Santa Cruz Biotechnology (Dallas, TX). Antibodies targeting AIMP3, IRS, and MRS were obtained from Santa Cruz Biotechnology. AIMP1 antibody was purchased from Proteintech (Rosemont, IL). Antibodies for KRS, PARP, β-actin, GAPDH, and caspase-3 were purchased from Cell Signaling (Danvers, MA). Goat anti-mouse or goat anti-rabbit IRDye®800CW (green) and IRDye®680RD (red) were obtained from LI-COR (Lincoln, NE). Alexa 488 goat anti-rabbit secondary antibody was purchased from Thermo Fisher Scientific. 3xFLAG and neoepitope-blocking peptide were synthesized by Sheldon Biotech (Montréal, Quebec, Canada) and Pierce, respectively. Active recombinant human caspase-1, -4, -6, and -10 were obtained from Enzo Life Sciences.

Cloning and constructs

For bacterial expression, $ERS^{2.5W}$ (corresponding to amino acids 1–929) and $PRS^{0.5W}$ (corresponding to amino acids 930–1512) were subcloned in pTrcHisB (Thermo Fisher Scientific) by PCR using human EPRS cDNA (Origene plasmid MR218237) as template and the restriction enzyme sites SacI and BstBI for $ERS^{2.5W}$ and BamHI and HindIII for $PRS^{0.5W}$. ERS (corresponding to amino acids 1–749) was cloned from $ERS^{2.5W}$ expression plasmid using Gibson Assembly (New England Biolabs, Ipswich, MA). Briefly, pTrcHisB-$ERS^{2.5W}$ was digested with AflII and BstBI, and a gBlock fragment containing a stop codon at residue 750 was used for Gibson assembly. For mammalian expression, EPRS and $PRS^{0.5W}$ (corresponding to amino acids 930–1512) were cloned into p3X-FLAG-CMV10 (Sigma) by PCR using NotI and XbaI. For p3X-FLAG-$ERS^{2.5W}$ (corresponding to amino acids 1–929), a point mutation was introduced at residue 930 to generate a stop codon using full-length p3X-FLAG-EPRS plasmid and PCR-based QuikChange site-directed mutagenesis kit (Agilent, Santa Clara, CA). Similarly, p3X-FLAG-$EPRS^{D929A}$ mutant was constructed by PCR using p3X-FLAG-EPRS as template and QuikChange site-directed mutagenesis. FLAG-linker-PRS (corresponding to amino acids 683–1512) and FLAG-PRS (corresponding to amino acids 1024–1512) were cloned into pcDNA3.1-myc-HisB vector by PCR using the EcoRV and XbaI restriction sites and with the N-terminal FLAG tag inserted using the 5′ primer. All *EPRS* constructs were verified by sequencing at the Lerner Research Institute Genomics Core. Caspase expression plasmids pET23b-Casp3-His (plasmid no. 11821) and pET23b-Casp7-His (plasmid no. 11825) were obtained from Addgene (Cambridge, MA).

Bioinformatic analysis

Human EPRS caspase cleavage site prediction was performed using the cascleave webserver (60) using NCBI reference sequence NP_004437.2. Conservation of caspase cleavage sites was determined using Clustal Omega and the following NCBI sequences: NP_004437.2; XP_001172425.1; NP_001230249.1; XP_012042445.1; XP_849468.1; NP_001019409.1; NP_084011.1; NP_001006398.1; NP_001121346.1; NP_001275581.1; NP_524471.2; NP_001022777.1; and NP_492711.1. Domains were shown to scale using DOG 2.0 illustrator software (61).

Transient transfections and cell culture treatment

HEK293F and N2a cells were transfected using polyethyleneimine as described (36) or Lipofectamine 2000 (Thermo Fisher Scientific) according to the manufacturer's instructions. Z-VAD-FMK was used at a concentration of 20 μM unless otherwise indicated. Apoptosis induction in HT29 cells was performed by combined treatment with TNFα (10 ng/ml) and cycloheximide (20 μg/ml) in the presence or absence of Z-VAD-FMK (40 μM) for the indicated times and TNFα-only treated cells were negative controls.

Mammalian protein expression and purification

FLAG-EPRS and $EPRS^{D929A}$ were expressed in HEK293F cells by transient transfection as described above. Cells were harvested 72 h after transfection in TNE lysis buffer supplemented with complete protease inhibitors (Roche Applied Science). Lysates were cleared by centrifugation at 16,000 $\times$ *g* for 20 min. Pulldown was performed overnight with Dynabeads protein-G (Thermo Fisher Scientific) coupled to anti-FLAG M2 antibody at 4 °C. Beads were washed three times with TNE buffer, and proteins were eluted with p3XFLAG peptide according to the manufacturer's protocol. Protein preparations were used fresh for subsequent assays.

Caspase cleavage assays

Cells were harvested in PhosphoSafe™ extraction buffer (EMD Millipore, Billerica, MA) supplemented with complete protease inhibitors (Roche Applied Science) and cleared by centrifugation at 16,000 $\times$ *g* for 20 min at 4 °C. Cell lysates (300 μg) expressing FLAG-EPRS (WT) or (D929A), or vector control, were treated with active recombinant caspase-3 (550 nM) in a total volume of 100 μl in caspase activity buffer (20 mM HEPES, pH 7.5, 100 mM NaCl, 10% sucrose, 0.1% CHAPS, and 10 mM DTT) for 3 h at 37 °C. For *in vitro* cleavage, 2 μg of purified FLAG-EPRS or $EPRS^{D929A}$ was incubated with 25 units of active recombinant caspase-1, -4, -6, or -10 or 550 nM active recombinant caspase-3 or -7 in caspase activity buffer for 4 h at 37 °C in a 50-μl reaction volume. Reactions were stopped by boiling in Laemmli buffer and analyzed by Western blotting.

Immunoprecipitation

For EPRS association with MSC components, HEK293F transfected with FLAG-EPRS or truncated variants were harvested in PhosphoSafe™ extraction buffer (EMD Millipore) 48 h after transfection and cleared by centrifugation at 16,000 $\times$ *g* for 20 min. Immunoprecipitation was performed overnight at 4 °C using 0.5 mg of lysates, 25 μl of protein-G Dynabeads, and FLAG M2 antibody at 1:100 dilution in a final volume of 0.5 ml. Beads were subsequently washed four times with 0.5 ml of PBS and boiled in Laemmli sample buffer, followed by Western blotting with antibodies for MSC components.

Downloaded from http://www.jbc.org/ at Rsch Cntr Julich Res library on November 22, 2018

Quantitative Western blotting

SDS-PAGE was performed using Tris-glycine or MOPS-based gels. Gels were subjected to transfer at 200 mA for 1 h at 4 °C using Immobilon-FL PVDF membranes (0.45 μm pore size) in Tris-glycine buffer (TBS) containing 20% methanol. Blots were blocked with 5% nonfat milk in TBS and immunoblotted with primary antibodies overnight at 4 °C. For detection, goat anti-mouse, goat anti-rabbit IRDye®800CW (green), or IRDye®680RD (red) were used at a 1:15,000 dilution in 5% milk in TBS supplemented with 0.1% Tween 20 (TBST) and 0.01% SDS. Blots were washed four times for 5 min in TBST followed by one wash in TBS, and visualized using the LI-COR Odyssey® CLx and ImageStudio software 3.1.4.

Generation and characterization of neoepitope antiserum

Antigenicity of neoepitope peptide ^{922}KAPKDQVD^{929} was assessed using antigen profiler tool from Thermo Fisher Scientific, and its unique presence in EPRS was verified by BLAST search of the human genome. High-purity peptide (>90%) was synthesized with N-terminal cysteine added for conjugation to keyhole limpet hemocyanin. Following conjugation, the peptide was dialyzed and used to immunize two rabbits. All neoepitope antibody production steps, including peptide synthesis, purification, conjugation, rabbit immunization, and bleed collection, were performed by Pierce. The optimal titer of the antiserum against the neoepitope peptide exceeded 1:200,000 by ELISA. Peptide-blocking experiments were performed on immunoblots of total N2a cell lysates expressing FLAG-EPRS, FLAG-ERS$^{2.5W}$, or vector constructs. Blocking peptide was diluted in blocking buffer (5% nonfat milk in TBST) at a final concentration of 10 μM and incubated with neoepitope antiserum (1:20,000) for 2 h at room temperature. Western blotting was performed overnight at 4 °C with neoepitope antiserum (1:20,000), with or without blocking peptide, and developed using standard procedures.

Immunofluorescence

Formalin-fixed, paraffin-embedded human colon tissue slides (HuFPT036) and tissue microarrays (FDA808c-01 and FDA808-c20) were obtained from US Biomax (Rockville, MD). Tissue sections were de-paraffinized and rehydrated in water. Antigen retrieval was avoided because it interfered with neoepitope antiserum immunoreactivity. Tissue sections were washed two times for 2 min in PBS containing 0.1% Tween followed by a 5-min wash in PBS. Nonspecific binding was reduced using blocking buffer (5% normal goat serum in PBS) for 1 h at room temperature. Colon sections were incubated with preimmune serum or neoepitope antiserum (1:50) overnight at 4 °C. Human tissue arrays were incubated with neoepitope antiserum only. Sections were washed three times for 10 min in PBS and probed with Alexa 488 goat anti-rabbit secondary antibody (1:300) in blocking buffer at room temperature. Following 1.5 h of incubation, sections were washed three times for 10 min in PBS and mounted using ProLong Gold anti-fade reagent (Thermo Fisher Scientific) containing 4′,6-diamidino-2-phenylindole (DAPI). Immunostaining was visualized on a wide-field Leica DM upright fluorescence microscope.

Recombinant protein expression and purification

ERS$^{2.5W}$, ERS, and PRS$^{0.5W}$ were expressed in BL21-CodonPlus (DE3)-RIPL at 37 °C and induced with 200 μM isopropyl β-D-1-thiogalactopyranoside. Cells were harvested by centrifugation 4 – 6 h after induction and lysed on ice in buffer A (50 mM Tris-HCl, pH 8.0, 100 mM NaCl, and 10% glycerol) supplemented with 1 mg/ml lysozyme, protease inhibitors, and 10 mM imidazole. Cells were sonicated on ice for 20 min and cleared by centrifugation at 26,000 × *g* for 45 min. Lysate was loaded onto a HisTrap HP column (GE Life Sciences, Pittsburgh, PA) pre-equilibrated with buffer A supplemented with 10 mM imidazole, washed with 15× column volume with equilibration buffer, followed by 15× column volume with buffer A supplemented with 20 mM imidazole, and eluted with a 20 –250 mM imidazole gradient. Peak fractions were dialyzed in buffer A and subsequently used for analysis of aminoacylation activity and for MST experiments. For SANS measurements, large-scale purification was performed as above. Following dialysis, protein was concentrated in a stirred cell, pressure-based concentration system (Millipore) and further purified by Superose 12 or Superdex 200 chromatography (GE Life Sciences) in buffer A. Fractions corresponding to monomeric protein were pooled and used for SANS measurements. For SANS analysis, absorbance of the purified proteins at 280 was determined using Nanodrop 2000 (Thermo Fisher Scientific) and was used with extinction coefficient to calculate the protein concentrations. For the aminoacylation activity reactions, protein concentrations were determined by Bradford assay. All purifications were performed using the Äkta purifier system (GE Life Sciences). Recombinant caspase-3 and -7 were purified as described (36).

Size-exclusion chromatography and BS^3 cross-linking

The oligomeric states of ERS$^{2.5W}$ and ERS were determined on a pre-calibrated analytical scale Superdex 200 column (GE Life Sciences). Column calibration and chromatography runs were performed in buffer A using gel-filtration standards (Bio-Rad) and ~150 μg of ERS$^{2.5W}$ or ERS. Peak elution profiles were analyzed by Unicorn 5.11 software (GE Life Sciences). For cross-linking, ERS$^{2.5W}$ and ERS (63 nM) and BS^3 cross-linker (127 nM) were dialyzed at room temperature for 30 min in buffer containing 50 mM HEPES, pH 8.0, and 100 mM NaCl in a total volume of 50 μl. Reactions were quenched with 100 mM Tris-HCl, pH 7.5, for 15 min, and proteins were analyzed on a 7.5% SDS-polyacrylamide gel and visualized with Imperial protein stain (Thermo Fisher Scientific) and a LICOR Odyssey scanner CLx.

Aminoacylation assay

Glutamyl-tRNA aminoacylation was measured in a 100-μl reaction volume in assay buffer (20 mM Tris-HCl, pH 7.5, 100 mM NaCl, 5 mM $MgCl_2$, 3 mM ATP, 1 mM DTT) supplemented with 30 μCi of L-[^{14}C]glutamate (PerkinElmer Life Sciences), and 500 μg of total yeast tRNA (Sigma). Prolyl-tRNA aminoacylation activity was measured in a 50-μl reaction volume in HEPES assay buffer (20 mM HEPES, pH 8.0, 100 mM NaCl, 5 mM $MgCl_2$, 3 mM ATP, and 1 mM DTT) supplemented with 150 μM L-[^{14}C]proline and 1 mg of total yeast tRNA. The reactions were preequilibrated to 30 °C prior to initiation by addition of

Downloaded from http://www.jbc.org/ at Rsch Cntr Julich Res library on November 22, 2018

$ERS^{2.5W}$ or $PRS^{0.5W}$ to final concentrations of 1 μM and 50 nM, respectively. Reactions were incubated at 30 °C, and 10- and 6-μl aliquots were collected for $ERS^{2.5W}$ or $PRS^{0.5W}$, respectively, at the times indicated and spotted on glass filters (Whatman GF/C™) presoaked with 5% trichloroacetic acid (TCA). Filters were washed 3× 1 ml with 5% TCA followed by 2× 1 ml washes with 100% ethanol. Filters were dried in hybridization oven at 60 °C for 10 min. Radioactivity on filters was quantified by liquid scintillation counting (TRI-CARB 1900TR, PerkinElmer Life Sciences).

SANS analysis

SANS experiments on $ERS^{2.5W}$ and ERS with and without ligand were carried out at Jülich Center for Neutron Sciences (Garching, Germany). The KWS1 SANS instrument is a classical pinhole camera providing a high neutron flux. Data were collected for 2 h from two detector positions 1.65 and 7.65 m from the sample and collimation lengths of 2 and 8 m, and covered a range of the scattering vector (Q) from 0.006 to 0.3 $Å^{-1}$ and neutron beam wavelength of 4.5 Å. $ERS^{2.5W}$ and ERS at concentrations of 28 and 70 μM, respectively, were measured at 6–8 °C in purification buffer supplemented with 5 mM $MgCl_2$ without ligand or in the presence of 5 mM L-Glu and ATP. Scattering intensity measurements of buffer only or buffer plus ligand were subtracted from the sample intensities. Samples with and without ligand received the same volume of purification buffer. The radius of gyration (R_g) for both proteins was obtained from the corresponding scattering intensity based on the Guinier approximation (62). SANS data were processed as follows: GNOM was used to de-convolute the scattering intensity curves into pair-distance distribution functions, $P(r)$ (63). GNOM also allows for data point exclusion at low angle and was used to determine the impact of minor aggregation on $ERS^{2.5W}$ $P(r)$ function. Subsequently, DAMMIN was used to produce 16 low-resolution structures for each macromolecule from its $P(r)$ function using simulated annealing (41). Finally, DAMAVER was used to build an average shape for each protein by extracting common structural features from the low-resolution structures. PyMOL was used to visualize the low-resolution structures and the average shape.

Composition analysis from SANS intensity

For a monodisperse sample, the SANS intensity at zero scattering angle ($I(q = 0)$ (cm^{-1})) is proportional to sample concentration (C) and biopolymer molecular mass (M) ($I(q = 0)$ = factor × C × M) (64). The proportionality factor depends on the average protein density and the scattering contrast, $\Delta\rho = \rho_{protein} - \rho_{buffer}$, where $\rho_{protein}$ and ρ_{buffer} are the scattering length densities (cm^{-2}) of the protein and the buffer, respectively. This proportionality relationship permits estimation of M when C and the type of biopolymer (*e.g.* protein, DNA) are known. However, in the case of a mixture, the total intensity at zero-scattering angle is the sum of intensities of the mixture components (65). When the sample is not monodisperse and contains the biopolymer in limited oligomerization states (*e.g.* monomer, dimer, etc.), and chemical identity of the monomer, M, and total C are known, the composition and the oligomerization state of the biopolymer can be determined from the scattering intensity at zero angle (forward intensity). Cross-linking electrophoretic gel analysis revealed the oligomeric states of $ERS^{2.5W}$ and ERS, and we calculated the forward scattering intensity using SANScript (65). SANScript uses amino acid composition, sample concentration, and an initial estimate of sample multimeric composition as input data to calculate the scattering intensity at zero angle.

Protein fluorescence spectroscopy

Intrinsic tryptophan fluorescence was measured at room temperature in purification buffer A using 100 nM $ERS^{2.5W}$ or ERS in a 100-μl volume using a Hellma Analytics SUPRASIL cell and PerkinElmer Life Sciences luminescence spectrometer (LS-50B). Data were collected using Fl WinLab software. Excitation wavelength was set to 295 nm, and emission was scanned between 310 and 400 nm. Data were corrected for baseline shifts and plotted using Prism 4 software (GraphPad).

Trypsin protection assay

Limited-trypsinization assay was done as described previously with modification (66). Reactions were performed at 37 °C in a total volume of 15 μl per time point, containing 5 μg of $ERS^{2.5W}$ or ERS and 20 ng of trypsin in purification buffer A. Reactions were stopped in 0.5 mM phenylmethylsulfonyl fluoride, boiled in Laemmli buffer, and analyzed by SDS-PAGE followed by quantitative Western blotting. Results were plotted using Prism 4 software.

MST

MST was used in experiments involving small molecule (ligand)–protein or protein–protein interactions to determine binding affinities or to analyze protein self-association. Recombinant purified $ERS^{2.5W}$ and ERS were labeled using cysteine-reactive red-maleimide labeling kit (NanoTemper, South San Francisco) according to the manufacturer's instructions. Unreacted dye was removed by buffer-exchange chromatography (EC), and labeled proteins were eluted in EC buffer containing 50 mM Tris-HCl, pH 8.0, 200 mM NaCl, 5 mM $MgCl_2$, and 10% glycerol. Binding assays were performed using MST premium-coated capillaries (NanoTemper). MST measurements were conducted with 33 and 5 nM labeled $ERS^{2.5W}$ and ERS, respectively, and the indicated amounts of ATP, tRNA, L-Glu, and unlabeled $ERS^{2.5W}$ or ERS in EC buffer. Measurements were made using the Monolith NT.115 (NanoTemper), and data were analyzed using MO.Affinity analysis (×64) software. Graphs were blotted using Prism 4 software.

Author contributions—D. H. developed reagents and performed all experiments with the exception of the SANS measurements, *ab initio* modeling, and SANScript computational analysis which were done by V. G., J. A. D., and V. P. D. H., V. G., and P. L. F. conceived experiments, analyzed data, and wrote the manuscript. P. Y., C. T., A. C., A. A., and K. V. contributed reagents and protocols to the study and contributed to data analysis. S. L. H. specifically contributed to the analysis and interpretation of the SANS data. All authors reviewed, edited, and approved the manuscript.

Downloaded from http://www.jbc.org/ at Rsch Cntr Julich Res library on November 22, 2018

References

1. Schimmel, P. (1987) Aminoacyl tRNA synthetases: general scheme of structure-function relationships in the polypeptides and recognition of transfer RNAs. *Annu. Rev. Biochem.* **56,** 125–158 CrossRef Medline
2. Ibba, M., and Soll, D. (2000) Aminoacyl-tRNA synthesis. *Annu. Rev. Biochem.* **69,** 617–650 CrossRef Medline
3. Ko, Y. G., Kim, E. Y., Kim, T., Park, H., Park, H. S., Choi, E. J., and Kim, S. (2001) Glutamine-dependent antiapoptotic interaction of human glutaminyl-tRNA synthetase with apoptosis signal-regulating kinase 1. *J. Biol. Chem.* **276,** 6030–6036 CrossRef Medline
4. Park, M. C., Kang, T., Jin, D., Han, J. M., Kim, S. B., Park, Y. J., Cho, K., Park, Y. W., Guo, M., He, W., Yang, X. L., Schimmel, P., and Kim, S. (2012) Secreted human glycyl-tRNA synthetase implicated in defense against ERK-activated tumorigenesis. *Proc. Natl. Acad. Sci. U.S.A.* **109,** E640–E647 CrossRef Medline
5. Yannay-Cohen, N., Carmi-Levy, I., Kay, G., Yang, C. M., Han, J. M., Kemeny, D. M., Kim, S., Nechushtan, H., and Razin, E. (2009) LysRS serves as a key signaling molecule in the immune response by regulating gene expression. *Mol. Cell* **34,** 603–611 CrossRef Medline
6. Sampath, P., Mazumder, B., Seshadri, V., Gerber, C. A., Chavatte, L., Kinter, M., Ting, S. M., Dignam, J. D., Kim, S., Driscoll, D. M., and Fox, P. L. (2004) Noncanonical function of glutamyl-prolyl-tRNA synthetase: gene-specific silencing of translation. *Cell* **119,** 195–208 CrossRef Medline
7. Jia, J., Arif, A., Ray, P. S., and Fox, P. L. (2008) WHEP domains direct noncanonical function of glutamyl-prolyl tRNA synthetase in translational control of gene expression. *Mol. Cell* **29,** 679–690 CrossRef Medline
8. Paukstelis, P. J., Chen, J. H., Chase, E., Lambowitz, A. M., and Golden, B. L. (2008) Structure of a tyrosyl-tRNA synthetase splicing factor bound to a group I intron RNA. *Nature* **451,** 94–97 CrossRef Medline
9. Han, J. M., Jeong, S. J., Park, M. C., Kim, G., Kwon, N. H., Kim, H. K., Ha, S. H., Ryu, S. H., and Kim, S. (2012) Leucyl-tRNA synthetase is an intracellular leucine sensor for the mTORC1-signaling pathway. *Cell* **149,** 410–424 CrossRef Medline
10. Bonfils, G., Jaquenoud, M., Bontron, S., Ostrowicz, C., Ungermann, C., and De Virgilio, C. (2012) Leucyl-tRNA synthetase controls TORC1 via the EGO complex. *Mol. Cell* **46,** 105–110 CrossRef Medline
11. Wakasugi, K., and Schimmel, P. (1999) Two distinct cytokines released from a human aminoacyl-tRNA synthetase. *Science* **284,** 147–151 CrossRef Medline
12. Turpaev, K. T., Zakhariev, V. M., Sokolova, I. V., Narovlyansky, A. N., Amchenkova, A. M., Justesen, J., and Frolova, L. Y. (1996) Alternative processing of the tryptophanyl-tRNA synthetase mRNA from interferon-treated human cells. *Eur. J. Biochem.* **240,** 732–737 CrossRef Medline
13. Lo, W. S., Gardiner, E., Xu, Z., Lau, C. F., Wang, F., Zhou, J. J., Mendlein, J. D., Nangle, L. A., Chiang, K. P., Yang, X. L., Au, K. F., Wong, W. H., Guo, M., Zhang, M., and Schimmel, P. (2014) Human tRNA synthetase catalytic nulls with diverse functions. *Science* **345,** 328–332 CrossRef Medline
14. Yao, P., Potdar, A. A., Arif, A., Ray, P. S., Mukhopadhyay, R., Willard, B., Xu, Y., Yan, J., Saidel, G. M., and Fox, P. L. (2012) Coding region polyadenylation generates a truncated tRNA synthetase that counters translation repression. *Cell* **149,** 88–100 CrossRef Medline
15. Guo, M., Schimmel, P., and Yang, X. L. (2010) Functional expansion of human tRNA synthetases achieved by structural inventions. *FEBS Lett.* **584,** 434–442 CrossRef Medline
16. Zhou, Q., Kapoor, M., Guo, M., Belani, R., Xu, X., Kiosses, W. B., Hanan, M., Park, C., Armour, E., Do, M. H., Nangle, L. A., Schimmel, P., and Yang, X. L. (2010) Orthogonal use of a human tRNA synthetase active site to achieve multifunctionality. *Nat. Struct. Mol. Biol.* **17,** 57–61 CrossRef Medline
17. Howard, O. M., Dong, H. F., Yang, D., Raben, N., Nagaraju, K., Rosen, A., Casciola-Rosen, L., Härtlein, M., Kron, M., Yang, D., Yiadom, K., Dwivedi, S., Plotz, P. H., and Oppenheim, J. J. (2002) Histidyl-tRNA synthetase and asparaginyl-tRNA synthetase, autoantigens in myositis, activate chemokine receptors on T lymphocytes and immature dendritic cells. *J. Exp. Med.* **196,** 781–791 CrossRef Medline
18. Raben, N., Nichols, R., Dohlman, J., McPhie, P., Sridhar, V., Hyde, C., Leff, R., and Plotz, P. (1994) A motif in human histidyl-tRNA synthetase which is shared among several aminoacyl-tRNA synthetases is a coiled-coil that is essential for enzymatic activity and contains the major autoantigenic epitope. *J. Biol. Chem.* **269,** 24277–24283 Medline
19. Xu, Z., Wei, Z., Zhou, J. J., Ye, F., Lo, W. S., Wang, F., Lau, C. F., Wu, J., Nangle, L. A., Chiang, K. P., Yang, X. L., Zhang, M., and Schimmel, P. (2012) Internally deleted human tRNA synthetase suggests evolutionary pressure for repurposing. *Structure* **20,** 1470–1477 CrossRef Medline
20. Grice, S. J., Sleigh, J. N., Motley, W. W., Liu, J. L., Burgess, R. W., Talbot, K., and Cader, M. Z. (2015) Dominant, toxic gain-of-function mutations in gars lead to non-cell autonomous neuropathology. *Hum. Mol. Genet.* **24,** 4397–4406 CrossRef Medline
21. Lee, J. Y., Kim, D. G., Kim, B. G., Yang, W. S., Hong, J., Kang, T., Oh, Y. S., Kim, K. R., Han, B. W., Hwang, B. J., Kang, B. S., Kang, M. S., Kim, M. H., Kwon, N. H., and Kim, S. (2014) Promiscuous methionyl-tRNA synthetase mediates adaptive mistranslation to protect cells against oxidative stress. *J. Cell Sci.* **127,** 4234–4245 CrossRef Medline
22. Freist, W., Gauss, D. H., Söll, D., and Lapointe, J. (1997) Glutamyl-tRNA synthetase. *Biol. Chem.* **378,** 1313–1329 Medline
23. Ray, P. S., and Fox, P. L. (2014) Origin and evolution of glutamyl-prolyl tRNA synthetase WHEP domains reveal evolutionary relationships within holozoa. *PLoS ONE* **9,** e98493 CrossRef Medline
24. Havrylenko, S., and Mirande, M. (2015) Aminoacyl-tRNA synthetase complexes in evolution. *Int. J. Mol. Sci.* **16,** 6571–6594 CrossRef Medline
25. Ward, J. R., Vasu, K., Deutschman, E., Halawani, D., Larson, P. A., Zhang, D., Willard, B., Fox, P. L., Moran, J. V., and Longworth, M. S. (2017) Condensin II and GAIT complexes cooperate to restrict LINE-1 retrotransposition in epithelial cells. *PLoS Genet.* **13,** e1007051 CrossRef Medline
26. Lee, E. Y., Lee, H. C., Kim, H. K., Jang, S. Y., Park, S. J., Kim, Y. H., Kim, J. H., Hwang, J., Kim, J. H., Kim, T. H., Arif, A., Kim, S. Y., Choi, Y. K., Lee, C., Lee, C. H., *et al.* (2016) Infection-specific phosphorylation of glutamyl-prolyl tRNA synthetase induces antiviral immunity. *Nat. Immunol.* **17,** 1252–1262 CrossRef Medline
27. Arif, A., Terenzi, F., Potdar, A. A., Jia, J., Sacks, J., China, A., Halawani, D., Vasu, K., Li, X., Brown, J. M., Chen, J., Kozma, S. C., Thomas, G., and Fox, P. L. (2017) EPRS is a critical mTORC1-S6K1 effector that influences adiposity in mice. *Nature* **542,** 357–361 CrossRef Medline
28. Mukhopadhyay, R., Jia, J., Arif, A., Ray, P. S., and Fox, P. L. (2009) The GAIT system: a gatekeeper of inflammatory gene expression. *Trends Biochem. Sci.* **34,** 324–331 CrossRef Medline
29. Arif, A., Jia, J., Mukhopadhyay, R., Willard, B., Kinter, M., and Fox, P. L. (2009) Two-site phosphorylation of EPRS coordinates multimodal regulation of noncanonical translational control activity. *Mol. Cell* **35,** 164–180 CrossRef Medline
30. Lei, H. Y., Zhou, X. L., Ruan, Z. R., Sun, W. C., Eriani, G., and Wang, E. D. (2015) Calpain cleaves most components in the multiple aminoacyl-tRNA synthetase complex and affects their functions. *J. Biol. Chem.* **290,** 26314–26327 CrossRef Medline
31. Shalak, V., Kaminska, M., Mitnacht-Kraus, R., Vandenabeele, P., Clauss, M., and Mirande, M. (2001) The EMAPII cytokine is released from the mammalian multisynthetase complex after cleavage of its p43/proEMAPII component. *J. Biol. Chem.* **276,** 23769–23776 CrossRef Medline
32. Dix, M. M., Simon, G. M., Wang, C., Okerberg, E., Patricelli, M. P., and Cravatt, B. F. (2012) Functional interplay between caspase cleavage and phosphorylation sculpts the apoptotic proteome. *Cell* **150,** 426–440 CrossRef Medline
33. Stoehr, G., Schaab, C., Graumann, J., and Mann, M. (2013) A SILAC-based approach identifies substrates of caspase-dependent cleavage upon TRAIL-induced apoptosis. *Mol. Cell. Proteomics* **12,** 1436–1450 CrossRef Medline
34. Shalini, S., Dorstyn, L., Dawar, S., and Kumar, S. (2015) Old, new and emerging functions of caspases. *Cell Death Differ.* **22,** 526–539 CrossRef Medline
35. Mort, J. S., Flannery, C. R., Makkerh, J., Krupa, J. C., and Lee, E. R. (2003) Use of anti-neoepitope antibodies for the analysis of degradative events in

Downloaded from http://www.jbc.org/ at Rsch Cntr Julich Res library on November 22, 2018

cartilage and the molecular basis for neoepitope specificity. *Biochem. Soc. Symp.* **2003,** 107–114 Medline

36. Halawani, D., Tessier, S., Anzellotti, D., Bennett, D. A., Latterich, M., and LeBlanc, A. C. (2010) Identification of caspase-6-mediated processing of the valosin containing protein (p97) in Alzheimer's disease: a novel link to dysfunction in ubiquitin proteasome system-mediated protein degradation. *J. Neurosci.* **30,** 6132–6142 CrossRef Medline
37. Grossmann, J., Mohr, S., Lapentina, E. G., Fiocchi, C., and Levine, A. D. (1998) Sequential and rapid activation of select caspases during apoptosis of normal intestinal epithelial cells. *Am. J. Physiol.* **274,** G1117–G1124 Medline
38. Grossmann, J., Walther, K., Artinger, M., Rümmele, P., Woenckhaus, M., and Schölmerich, J. (2002) Induction of apoptosis before shedding of human intestinal epithelial cells. *Am. J. Gastroenterol.* **97,** 1421–1428 CrossRef Medline
39. Krajewska, M., Wang, H. G., Krajewski, S., Zapata, J. M., Shabaik, A., Gascoyne, R., and Reed, J. C. (1997) Immunohistochemical analysis of in vivo patterns of expression of CPP32 (caspase-3), a cell death protease. *Cancer Res.* **57,** 1605–1613 Medline
40. Rambo, R. P., and Tainer, J. A. (2013) Accurate assessment of mass, models and resolution by small-angle scattering. *Nature* **496,** 477–481 CrossRef Medline
41. Svergun, D. I. (1999) Restoring low resolution structure of biological macromolecules from solution scattering using simulated annealing. *Biophys. J.* **76,** 2879–2886 CrossRef Medline
42. He, R., Zu, L. D., Yao, P., Chen, X., and Wang, E. D. (2009) Two non-redundant fragments in the N-terminal peptide of human cytosolic methionyl-tRNA synthetase were indispensable for the multi-synthetase complex incorporation and enzyme activity. *Biochim. Biophys. Acta* **1794,** 347–354 CrossRef Medline
43. Chang, C. Y., Chien, C. I., Chang, C. P., Lin, B. C., and Wang, C. C. (2016) A WHEP domain regulates the dynamic structure and activity of *Caenorhabditis elegans* glycyl-tRNA synthetase. *J. Biol. Chem.* **291,** 16567–16575 CrossRef Medline
44. Qin, X., Deng, X., Chen, L., and Xie, W. (2016) Crystal structure of the wildtype human GlyRS bound with tRNA(Gly) in a productive conformation. *J. Mol. Biol.* **428,** 3603–3614 CrossRef Medline
45. Guo, M., Yang, X. L., and Schimmel, P. (2010) New functions of aminoacyl-tRNA synthetases beyond translation. *Nat. Rev. Mol. Cell Biol.* **11,** 668–674 CrossRef Medline
46. Jeong, E. J., Hwang, G. S., Kim, K. H., Kim, M. J., Kim, S., and Kim, K. S. (2000) Structural analysis of multifunctional peptide motifs in human bifunctional tRNA synthetase: identification of RNA-binding residues and functional implications for tandem repeats. *Biochemistry* **39,** 15775–15782 CrossRef Medline
47. Burgon, P. G., and Megeney, L. A. (2017) Caspase signaling, a conserved inductive cue for metazoan cell differentiation. *Semin. Cell Dev. Biol.* **2017,** S1084–9521(17)30111–8 CrossRef Medline
48. Zhou, H., Sun, L., Yang, X. L., and Schimmel, P. (2013) ATP-directed capture of bioactive herbal-based medicine on human tRNA synthetase. *Nature* **494,** 121–124 CrossRef Medline
49. Cho, H. Y., Maeng, S. J., Cho, H. J., Choi, Y. S., Chung, J. M., Lee, S., Kim, H. K., Kim, J. H., Eom, C. Y., Kim, Y. G., Guo, M., Jung, H. S., Kang, B. S., and Kim, S. (2015) Assembly of multi-tRNA synthetase complex via heterotetrameric glutathione transferase-homology domains. *J. Biol. Chem.* **290,** 29313–29328 CrossRef Medline
50. Rho, S. B., Lee, J. S., Jeong, E. J., Kim, K. S., Kim, Y. G., and Kim, S. (1998) A multifunctional repeated motif is present in human bifunctional tRNA synthetase. *J. Biol. Chem.* **273,** 11267–11273 CrossRef Medline
51. Rho, S. B., Lee, K. H., Kim, J. W., Shiba, K., Jo, Y. J., and Kim, S. (1996) Interaction between human tRNA synthetases involves repeated sequence elements. *Proc. Natl. Acad. Sci. U.S.A.* **93,** 10128–10133 CrossRef Medline
52. Han, J. M., Lee, M. J., Park, S. G., Lee, S. H., Razin, E., Choi, E. C., and Kim, S. (2006) Hierarchical network between the components of the multi-tRNA synthetase complex: implications for complex formation. *J. Biol. Chem.* **281,** 38663–38667 CrossRef Medline
53. Dias, J., Renault, L., Pérez, J., and Mirande, M. (2013) Small-angle X-ray solution scattering study of the multi-aminoacyl-tRNA synthetase complex reveals an elongated and multi-armed particle. *J. Biol. Chem.* **288,** 23979–23989 CrossRef Medline
54. Ratinaud, M. H., Thomes, J. C., and Julien, R. (1983) Glutamyl-tRNA synthetases from wheat. Isolation and characterization of three dimeric enzymes. *Eur. J. Biochem.* **135,** 471–477 CrossRef Medline
55. Thomes, J. C., Ratinaud, M. H., and Julien, R. (1983) Dimeric glutamyl-tRNA synthetases from wheat. Kinetic properties and functional structures. *Eur. J. Biochem.* **135,** 479–484 CrossRef Medline
56. He, W., Bai, G., Zhou, H., Wei, N., White, N. M., Lauer, J., Liu, H., Shi, Y., Dumitru, C. D., Lettieri, K., Shubayev, V., Jordanova, A., Guergueltcheva, V., Griffin, P. R., Burgess, R. W., *et al.* (2015) CMT2D neuropathy is linked to the neomorphic binding activity of glycyl-tRNA synthetase. *Nature* **526,** 710–714 CrossRef Medline
57. Wakasugi, K., Slike, B. M., Hood, J., Otani, A., Ewalt, K. L., Friedlander, M., Cheresh, D. A., and Schimmel, P. (2002) A human aminoacyl-tRNA synthetase as a regulator of angiogenesis. *Proc. Natl. Acad. Sci. U.S.A.* **99,** 173–177 CrossRef Medline
58. Otani, A., Slike, B. M., Dorrell, M. I., Hood, J., Kinder, K., Ewalt, K. L., Cheresh, D., Schimmel, P., and Friedlander, M. (2002) A fragment of human TrpRS as a potent antagonist of ocular angiogenesis. *Proc. Natl. Acad. Sci. U.S.A.* **99,** 178–183 CrossRef Medline
59. Sekine, S., Nureki, O., Dubois, D. Y., Bernier, S., Chênevert, R., Lapointe, J., Vassylyev, D. G., and Yokoyama, S. (2003) ATP binding by glutamyl-tRNA synthetase is switched to the productive mode by tRNA binding. *EMBO J.* **22,** 676–688 CrossRef Medline
60. Song, J., Tan, H., Shen, H., Mahmood, K., Boyd, S. E., Webb, G. I., Akutsu, T., and Whisstock, J. C. (2010) Cascleave: towards more accurate prediction of caspase substrate cleavage sites. *Bioinformatics* **26,** 752–760 CrossRef Medline
61. Ren, J., Wen, L., Gao, X., Jin, C., Xue, Y., and Yao, X. (2009) DOG 1.0: illustrator of protein domain structures. *Cell Res.* **19,** 271–273 CrossRef Medline
62. Guinier, A. (1938) The diffusion of X-rays under the extremely weak angles applied to the study of fine particles and colloidal suspension. *C. R. Hebd. Seances Acad. Sci.* **206,** 1374–1376
63. Svergun, D. I. (1992) Determination of the regularization parameter in indirect-transform methods using perceptual criteria. *J. Appl. Crystallogr.* **25,** 495–503 CrossRef
64. Serdyuk, I. N., and Zaccai, Z. N. (2007) in *Methods in Molecular Biophysics* (Halliday, K., ed) pp. 423–455, Cambridge University Press, Cambridge, UK
65. Jacrot, B., and Zaccai, G. (1981) Determination of molecular weight by neutron scattering. *Biopolymers* **20,** 2413–2426 CrossRef
66. Halawani, D., LeBlanc, A. C., Rouiller, I., Michnick, S. W., Servant, M. J., and Latterich, M. (2009) Hereditary inclusion body myopathy-linked p97/VCP mutations in the NH2 domain and the D1 ring modulate p97/VCP ATPase activity and D2 ring conformation. *Mol. Cell. Biol.* **29,** 4484–4494 CrossRef Medline

Downloaded from http://www.jbc.org/ at Rsch Cntr Julich Res library on November 22, 2018

Structural control of caspase-generated glutamyl-tRNA synthetase by appended noncatalytic WHEP domains

Dalia Halawani, Valentin Gogonea, Joseph A. DiDonato, Vitaliy Pipich, Peng Yao, Arnab China, Celalettin Topbas, Kommireddy Vasu, Abul Arif, Stanley L. Hazen and Paul L. Fox

J. Biol. Chem. 2018, 293:8843-8860.
doi: 10.1074/jbc.M117.807503 originally published online April 11, 2018

Access the most updated version of this article at doi: 10.1074/jbc.M117.807503

Alerts:
- When this article is cited
- When a correction for this article is posted

Click here to choose from all of JBC's e-mail alerts

This article cites 65 references, 22 of which can be accessed free at
http://www.jbc.org/content/293/23/8843.full.html#ref-list-1

Downloaded from http://www.jbc.org/ at Rsch Cntr Julich Res library on November 22, 2018